Computers and Structures 309 (2025) 107652

Contents lists available at ScienceDirect

Computers and Structures

journal homepage: www.elsevier.com/locate/compstruc

# Shape monitoring of morphing wing structures using the inverse Finite Element Method

Vincenzo Biscotti *, Rinto Roy, Marco Gherlone

*Department of Mechanical and Aerospace Engineering, Politecnico di Torino, Corso Duca degli Abruzzi 24, Torino, 10129, Italy*

ARTICLE INFO

*Keywords:*
Morphing wing
Inverse Finite Element Method
Closed-loop control
Shape sensing
Strain sensors

ABSTRACT

This work presents a closed-loop control strategy for morphing wing structures where the feedback originates from monitoring the actual deformed shape of the morphed skin. The approach is based on the inverse Finite Element Method (iFEM), able to reconstruct the displacement field of a structure by minimizing, in a least squares sense, the error between the analytical strains and those experimentally measured in some discrete locations. Once the actual shape has been reconstructed, the actuation loads required to achieve the target shape are computed. The iFEM-based control strategy is assessed numerically on the example problem of a wing segment whose trailing-edge camber is modified via the morphing strategy. Actuation loads are represented by concentrated forces or by a distributed pressure, the effect of aerodynamic loads is taken into account, and strain data are measured on the top and bottom morphing skin. The results show accurate convergence to the target shape, thus demonstrating the potential of the proposed control-loop strategy.

## 1. Introduction

The term “morphing” is short for metamorphose, i.e., gradual transformation [1]. In morphing aircraft, this transformation revolves around the external shape of the aircraft, frequently of the wing [2], with the objective of providing high performance during different and even contrasting mission operations. The research field on morphing aircraft is brimming with a multitude of solutions and, in just the last few years, different reviews of this broad literature have been published [3–5]. The review of Ameduri and Concilio [5], in particular, highlights the numerous advantages, both in terms of performance and environmental impact of morphing wing structures, stressing the competitive edge of morphing solutions in the modern aerospace industry: their transversality, i.e., the capability to positively impact multiple aircraft systems, thus achieving widespread efficiency. Morphing capabilities and their potential always fascinated aircraft designers. For instance, the Wright Brothers developed their first design, the Wright Glider, exploiting morphing for lateral control, in an attempt to imitate the flight of buzzards [6]. However, throughout aviation history, developing a completely reliable, safety-compliant morphing structure proved to be a difficult task and prevented the large-scale diffusion of morphing applications. For this reason, in its Morphing Aircraft project, NASA advocated for the development of new and potentially disruptive technologies that would allow the realization of a full-performing morphing aircraft [7]. Since then, many innovative solutions have been proposed, mainly involving the design and production process, the actuation system, and the control loop architecture.

For the production and development of the morphing wing structure, Jennet et al. [8] designed a digital cellular solid structure. Cellular solids are materials made of a lattice array of 1D and 2D elements. The digital approach introduces in the cellular solid network a repetitive unit, which constitutes the building block element from which the entire structure is assembled. This strategy allows to drastically reduce the manufacturing process complexity and to precisely tune the properties of the cellular solid, which depend on the geometry of the lattice array. Another solution in the field of morphing aircraft manufacturing is the one proposed by De Gaspari et al. [9], and by Fasel et al. [10], who employed additive manufacturing to build the compliant structures of their morphing wing designs. This innovative process is economically affordable, as waste material is minimized and the complexity of the printed part does not increase the cost of the process. Furthermore, in the case of a composite fiber-reinforced structure, such as the one developed by Fasel et al. [10], the 3D printing technique allows to exploit the anisotropy of the material, by aligning the fibers in the direction of the load path.

* Corresponding author.
*E-mail address:* vincenzo.biscotti@polito.it (V. Biscotti).

https://doi.org/10.1016/j.compstruc.2025.107652
Received 7 March 2024; Accepted 17 January 2025
Available online 30 January 2025

To enable the actuation of the morphing wing structure, two main strategies are found in the literature: for morphing wings based on a rigid link mechanism, where the structure acts in a finger-like configuration [11,12], electromechanical actuators have been the privileged solution. On the other end, when developing ultralight-compliant designs, many researchers have explored the use of smart materials, namely piezoelectric and shape memory alloy (SMA) actuators [13–19]. In particular, De Breuker et al. [13] coupled piezoelectric bimorphs with electromechanical actuators to achieve faster morphing. On the other end, Molinari et al. [14] combined piezoelectric bimorphs with a skin made of dielectric elastomers, whereas in [15–17], Macro Fiber Composite (MFC) piezoelectric patches on the skin were used. In their work, Grigorie et al. [18], achieved the deformation of the upper skin surface using the action of Ni-Ti SMAs, in order to control the position of the transition point over the profile. Lastly, Jodin et al. [19] used the combination of SMA wires and MFC patches to obtain both large deformations at limited frequencies and high deformations at higher frequencies.

Another enabling technology for morphing wing structures is their control system, which, in turn, requires the development of an accurate, real-time feedback strategy: for the “finger-like” morphing structures, the feedback is frequently provided by measuring the relative rotations between the links with encoders [11,12]. In particular, Dimino et al. [12] coupled the encoders with chord-wise and span-wise strain measurements, to verify the compliance of the strain distribution with that of the target shape in specific points of interest. Strain sensors were also used by Nazeer et al. [20], in the form of FBG sensors, and by Molinari et al. [15] and Jodin et al. [19] as well, with both employing strain gauges. Notably, Nazeer et al. [20] converted the strain measurements into the tip displacement using appropriate transfer functions whereas, for the latter two, the strain data were directly fed to a PI controller to monitor the local deflection. In addition to the strain sensor information, Jodin et al. [19] also employed thermocouples to retrieve the SMA wire’s temperatures to use them as feedback in their control architecture. A similar solution was adopted by Grigorie et al. [18], as the displacements of two position transducers were used together with the temperature measurements as feedback for a fuzzy logic-based PID controller to monitor the shape variation of their morphing wing. Conversely, Haughn et al. [16] built an inference model with neural networks and coupled it with the internal displacements measured by flex sensors to reconstruct the tip deflection of the wing, which was then fed back to a reinforcement learning controller. Local displacement measurements, retrieved at specific locations through laser sensors, were also employed by Fichera et al. [17] in their camber morphing design.

A common feature of all the feedback shape control strategies discussed so far is that they all aim to monitor and act on the shape they control by either employing sensor measurements that are indirectly related to the displacements of the structure, as in the case of the relative rotations between the hinges of the actuators [11,12], which do not involve reconstructing the global morphed shape, or by using sensor measurements that are directly related to the displacements, such as the strain measurements or the displacements themselves, but that are exploited only for local reconstructions [15–17,20] (few strategies [18,19] implement hybrid solutions between these two approaches). This observation holds even when considering the broader, more comprehensive literature review on closed-loop shape control architectures for morphing wing structures by Parancheerivilakkathil et al. [21]. The review provides additional examples of local shape reconstructions through sensor measurements directly related to the local displacements, such as the twist angle of the twist morphing design of Sun et al. [22]. Also reviewed are applications employing sensor measurements only indirectly related to the displacements of the monitored structures. Examples include the torque in the actuation shafts of Kammegne et al. [23] and the motor speed in the application by Khan et al. [24]. In the latter, as well as in the one developed by Botez et al. [25] and Popov et al. [26], the linear actuator position was also measured. Furthermore, both Botez et al. and Khan et al. employed current measurements as feedback, while the pressure distribution was used by Popov et al. as a further feedback parameter. The pressure distribution was also employed in other closed-loop control strategies, for instance, in the one by Coutu et al. [27] where it allowed to compute the lift-to-drag ratio, or in the one by Kammegne et al. [28], where it was used to adjust the thickness of the morphing skin in order to monitor the transition point over the airfoil. These feedback strategies enable robust and effective control for the morphing wing designs examined, where morphing is employed to modify only one structural parameter of the wing (e.g. camber, thickness, skin contour). However, as highlighted by Parancheerivilakkathil et al. in their review [21], the most recent efforts in morphing wing designs have been concentrated in developing polymorphing wings, where multiple combinations of displacements and displacement rates are combined to act on the different structural parameters. As advocated in [21], polymorphing wings require proper control and feedback strategies that are not limited to one optimal morphing configuration and to one specific task. That is, local reconstruction of the structural parameters may be insufficient for these morphing designs. Furthermore, even sensor measurements indirectly related to displacements may be insufficient for future morphing wings. Ciminello et al. [29] stressed the relevance of an accurate and effective sensor network and shape feedback strategy: the complete knowledge of the global wing shape plays, in fact, a decisive role in the real-time evaluation of the commands provided by the control system and it also represents an instrumental factor in the evaluation of the improvements provided by the morphing solutions. Ciminello et al. [29] proposed a solution that represents an exception when considering the broad literature of feedback strategies previously examined: in their morphing design, they employed FBG sensors, i.e. sensor measurements directly related to the displacements, to provide the global reconstruction of the shape of their morphing trailing edge wing. In particular, to circumvent the problems related to the high strain levels in the chord-wise direction and the difficulties regarding the installation of the optical fibers on the skin of the structure, they designed two different solutions: a sliding bending beam device, acting as a transducer for the chord-wise strains, and thin flexible GFRP patches embedding the optical fibers for the strains measured along the span. To reconstruct the deformed shape, the polynomial interpolation of the strain measurements is combined with the integration of the classical beam strain-displacement relations. Recently, a similar strategy to the one proposed by Ciminello et al. was successfully tested on a ground demonstrator platform by Shi et al. [30]. Despite these promising results, as Ciminello et al. observed in their paper [29], the procedure is able to reconstruct only the flap mid-line, thus lacking the capability of monitoring the external shape of the morphing wing. A solution to this problem can be found in a recent work [31], where Roy et al. developed wing-structure open and closed-loop control strategies with feedback based on a shape-sensing approach.

A rapidly increasing interest is being devoted to shape-sensing approaches, i.e., methodologies to evaluate the global deformed shape of a structure starting from discrete strain measurements [32]. The reconstructed displacements can be further elaborated to obtain the strain and stress fields over the whole structural domain (thus enabling the application of Structural Health Monitoring approaches and more cost-efficient maintenance strategies based on actual data [33]). Shape sensing approaches are typically based on strain measurements and on related sensors. Apart from traditional strain gauges or rosettes, still applicable to laboratory experimental campaigns but less suitable for on-board monitoring, new sensors are gaining increasing popularity as Fiber Bragg Grating (FBG) sensors [34] and fiber-optical sensors based on Rayleigh scattering and Optical Frequency Domain Reflectometry [35].

Available shape-sensing approaches are usually classified into four categories [32]: (1) methods based on neural networks, (2) methods based on the integration of strains, (3) methods based on global or piecewise basis functions, and (4) methods relying on a FE-based variational principle. The main outcome of the efforts belonging to category (1) is

that the accuracy is strongly affected by the choice of training load cases [36].

Methodologies belonging to category (2) are typically developed for beam-like structures as in Ko's Displacement Theory [37]. The key idea is that axial strains measured along a "sensing line", with a known distance from the neutral axis of the beam, are integrated twice to obtain the deflection [37]. Further to simple bending, torsional deformation can be reconstructed by either using sensors oriented along the 45°-direction or by adopting a two-line strain-sensing system. Geometric complexities (tapered beams, sweep angles) can be taken into account by this methodology whose main application is for wing-structures deformed shape reconstruction [34,38].

Methods grouped into category (3) assume that the displacement field of a structure can be expressed in terms of known spatial functions and unknown coefficients whose value is determined in order to fit the reconstructed strains to the experimental ones. In particular, the Modal Method uses numerical or experimental mode shapes as spatial functions [39,40] and does not require any information on the applied loads. On one hand, the evaluation of the mode shapes often results in an onerous process and an energy-based criterion is therefore necessary to select those that mainly participate in the reconstruction of the displacement field [41]. On the other hand, the search for an optimal sensor configuration can lead to accurate results even when few strain data are available [42].

Among shape-sensing approaches formulated with FE-based variational principles (4), the so-called inverse Finite Element Method (iFEM) has recently gained increasing popularity in the scientific community. iFEM is founded on minimizing a weighted-least-squares functional measuring the error between the strains due to the reconstructed displacements (discretized using finite elements) and the strains experimentally measured in some discrete locations [43]. The formulation is only based on the strain-displacement relations, thus requiring no information on materials or loading conditions. iFEM was originally introduced for thin-walled structures, by adopting the kinematic assumptions of the First-order Shear Deformation Theory and consequently developing a three-node, triangular inverse shell element (iMIN3) [43,44]. More recently, a four-node, quadrilateral inverse shell element (iQS4) was proposed [45]. A class of one-dimensional inverse elements based on the Timoshenko beam theory was also formulated for truss and beam structures [46] and further extended to beams with complex cross-sections [47]. Moreover, recently a 1D inverse element was introduced combining iFEM with the Global Beam Theory to model cylindrical and conical shells [48,49]. Hybrid iFEM strategies (beam and shell inverse finite elements) have been successfully applied to stiffened structures [50]. iFEM has been shown to be general enough, thus leading to applications in several fields, ranging from aircraft structures [51–53], to marine structures [54,55] and civil structures [56,57]. Further, iFEM developments have been non-linear formulations for large displacements [58,59], special enhancements for multilayered composite and sandwich structures with highly heterogeneous stacking sequences [60,61], and iFEM-based approaches to damage-detection [62–64].

The capability to monitor the global shape of a structure in real-time and on-board, even when applied loads are unavailable or difficult to measure (e.g., aerodynamic forces) and when material data are either affected by uncertainties or unknown, represents a strategic advantage of the inverse Finite Element Method. At the same time, current feedback strategies relying on measured quantities indirectly related to the shape of the structure (i.e. not reconstructing the shape), or only based on local information of the morphed shape may be insufficient when considering the future polymorphing wing designs. Thus, the main objective of the present effort is to exploit the global shape reconstruction capabilities of the iFEM to fill this gap in the literature on morphing shape control architectures. Further developing the approach proposed by Roy et al. in [31], a closed-loop control strategy for a morphing wing structure where the feedback is coming from the iFEM providing the actual global deformed shape through discrete sensor strain measurements is realized, and its feasibility and efficacy are investigated at a numerical level. The paper is structured as follows: Section 2 provides a description of the wing structure and of the FE model used to simulate its response to actuation and aerodynamic loads. Section 3 describes the steps and ingredients of the control loop strategy. Section 4 summarizes the main assumptions and equations of iFEM, thus setting the numerical framework for the investigation. Section 5 presents and discusses the numerical results. Section 6 collects some general observations on the obtained results and provides some perspectives on future further investigations.

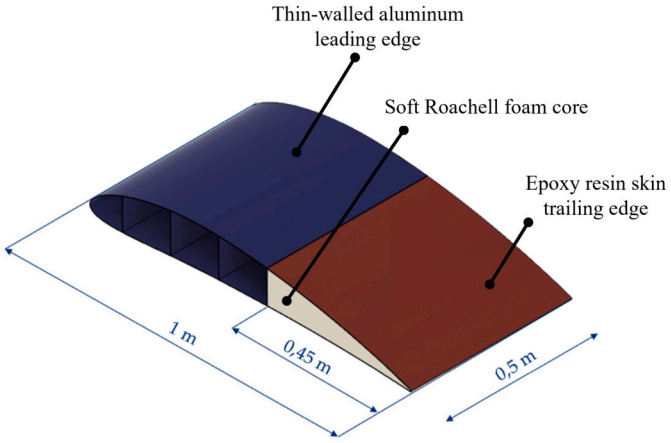


**Fig. 1.** Morphing wing structure.

## 2. The morphing wing model

This Section provides a description of the wing structure with the morphing trailing edge being considered for the investigation, and the FE model developed to simulate its structural behavior.

### 2.1. Morphing wing structure

To test the iFEM feedback-based closed-loop architecture, a morphing wing model is created. In the literature, camber morphing is the prevalent solution for morphing wing design, as it has shown the most promising results when evaluated both in terms of control capability and aerodynamic efficiency [16]. Among the camber morphing wings, the morphing trailing edge concepts have proven to be superior with respect to the corresponding leading edge designs [14]. Therefore, morphing capabilities are concentrated in the trailing edge of the tested wing and morphing is used only to change the camber of the trailing edge profile.

The morphing wing model is shown in Fig. 1. A NACA 6516 airfoil is chosen as the wing profile and the design represents a simplification of the morphing wing presented in [14]. The wing structure is divided into two parts: the first one is the leading edge (represented in blue), made of aluminum, thin-walled structures. This portion of the wing is considered infinitely rigid compared with the morphing trailing edge, which has a skin made of epoxy resin (represented in red) reinforced by a soft foam core. The materials used for the morphing portion of the wing are chosen so that the structure is compliant enough to exhibit morphing capabilities but, at the same time, has the strength to withstand the applied loads. In particular, the foam core is used to counteract the aerodynamic pressure distribution on the flexible skin of the trailing edge, which would otherwise deform excessively under this transverse action. The material properties and the thickness of the skin and core of the morphing trailing edge are summarized in Table 1. Both the epoxy skin and the foam core, as clearly shown by the data in the table, are considered as isotropic materials. This simplifying assumption facilitates the

**Table 1**
Materials and thickness data of the morphing wing model.

| | Trailing edge | |
|---|---|---|
| | Skin | Core |
| Material | Epoxy resin | Roachell WF 51 |
| E [MPa] | 3.2 | 75 |
| $\nu$ | 0.35 | 0.44 |
| thickness [mm] | 5 | 130 - 3 |

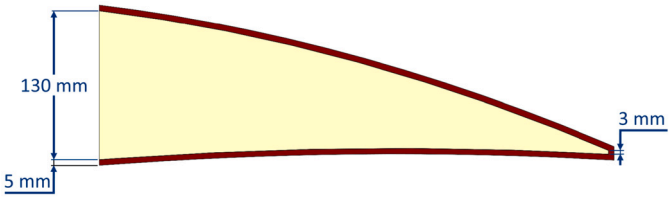


**Fig. 2.** Morphing trailing edge structure.

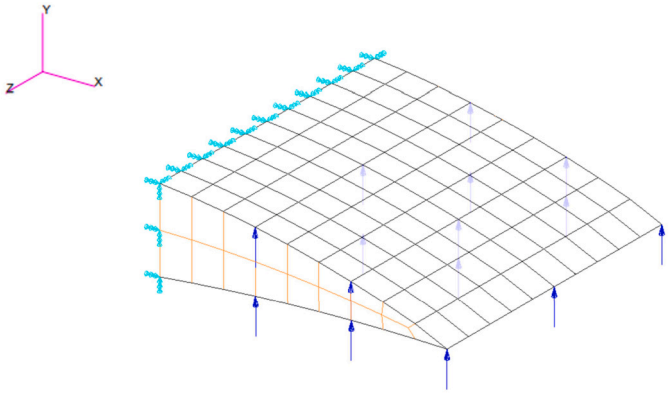


**Fig. 3.** Trailing edge FE model.

FEM implementation of the 3D model. The two thickness values provided for the core represent, respectively, the thickness of the portion of the core adjacent to the leading edge, and the thickness of the core at the trailing edge tip, as shown in Fig. 2.

### 2.2. The FE model

In the absence of an experimental model, a finite element model of the morphing wing structure is developed in order to simulate the structural behavior under the actuation loads and provide the simulated experimental strains required for the iFEM feedback-based control strategy. The FE model is presented in Fig. 3. Only the trailing edge structure, whose dimensions are displayed in Figs. 1 and 2, is modeled. The leading edge, instead, is represented by the clamped front end of the trailing edge. This choice is coherent with the assumption that the leading edge, made of aluminum, thin-walled structures, is infinitely rigid in comparison with the compliant morphing trailing edge.

The upper and lower skin surfaces of the trailing edge are modeled with 180 Quad4 2D shell elements, whereas 170 Hex8 solid elements are used for the foam core. The average global edge length of the elements is set at 0.005 m, resulting in a total of 308 nodes, of which 260 belong to the skin. Here the variables $N_{e,s}$ and $N_{e,f}$ are introduced to represent the number of elements in the skin and core, whereas $N_{n,s}$

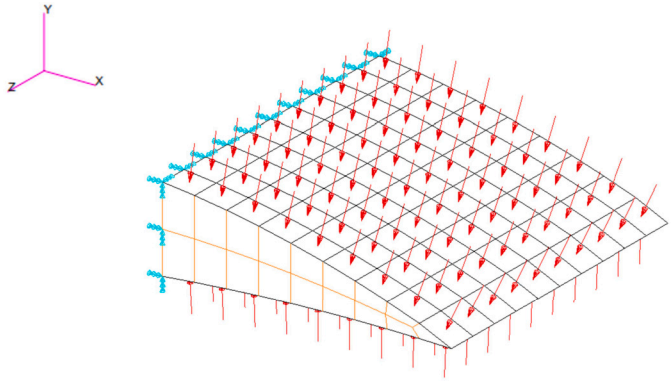


**Fig. 4.** Distributed pressure actuation scheme.

is used as the number of nodes in the skin. The FE model is developed using MSC/PATRAN and MSC/NASTRAN [65].

In Fig. 3, the tested actuation scheme is also shown: it consists of a set of transverse concentrated forces, that is, forces acting along the $Y$-direction (henceforth, the capital letter will be used to refer to the global reference system, which is shown in the top-left corner of Fig. 3), distributed both along the chord and along the span-wise direction. This actuation scheme may represent an extreme simplification of the action exerted by the piezoelectric or shape memory alloy actuators frequently used in modern morphing structures. However, this choice does not invalidate the results nor the procedure presented hereafter, as the objective of the paper is to test the iFEM feedback-based closed-loop strategy, rather than focusing on the creation of a high-fidelity model of the morphing wing architecture. Furthermore, this actuation scheme may be reproducible with the concept proposed by Berton [66], where the elongation and contraction of the SMA wires are converted through a mechanical link into a transverse action on the controlled surface. Similarly, the solution proposed by Wang et al. [67] could be employed to generate a set of distributed transverse loads: in order to drive their trailing edge morphing concept, Wang et al. coupled piezoelectric ultrasonic motors to an eccentuator, that is, a bending beam able to convert rotations at one end into vertical and lateral motions at the other. Taking inspiration from Wang et al. [67], a second actuation scheme, Fig. 4, employed to draw comparative results with the previous one, is considered. It consists of a set of distributed pressure loads acting perpendicularly on each element of the top and bottom skin of the trailing edge. The distributed pressure actuation scheme is modeled by applying an external pressure load on all the $N_{e,s}$ elements of the skin.

## 3. Control loop architecture

This Section presents the closed-loop control strategy that was implemented to control the shape of the morphing wing described in Section 2.

### 3.1. Notation

The shape of the structure is denoted by **P**, with different subscripts according to the particular shape being considered:

- $\mathbf{P}_{\mathbf{tgt}}$ is the target shape;
- $\mathbf{P}_{\mathbf{iFEM}}$ is the iFEM reconstructed shape;
- $\mathbf{P}_{\mathbf{FEM}}$ is the shape obtained using the FE Model of the structure.

The shape is defined in terms of displacements. Thus, **P** is a matrix containing the nodal displacement components $(u_X, u_Y, u_Z)$ defined with respect to the unmorphed shape in the global coordinate system. In particular, **P** is a $N_{n,s}$ x 3 matrix whose rows correspond to the $N_{n,s}$ nodes of the FE modeled skin

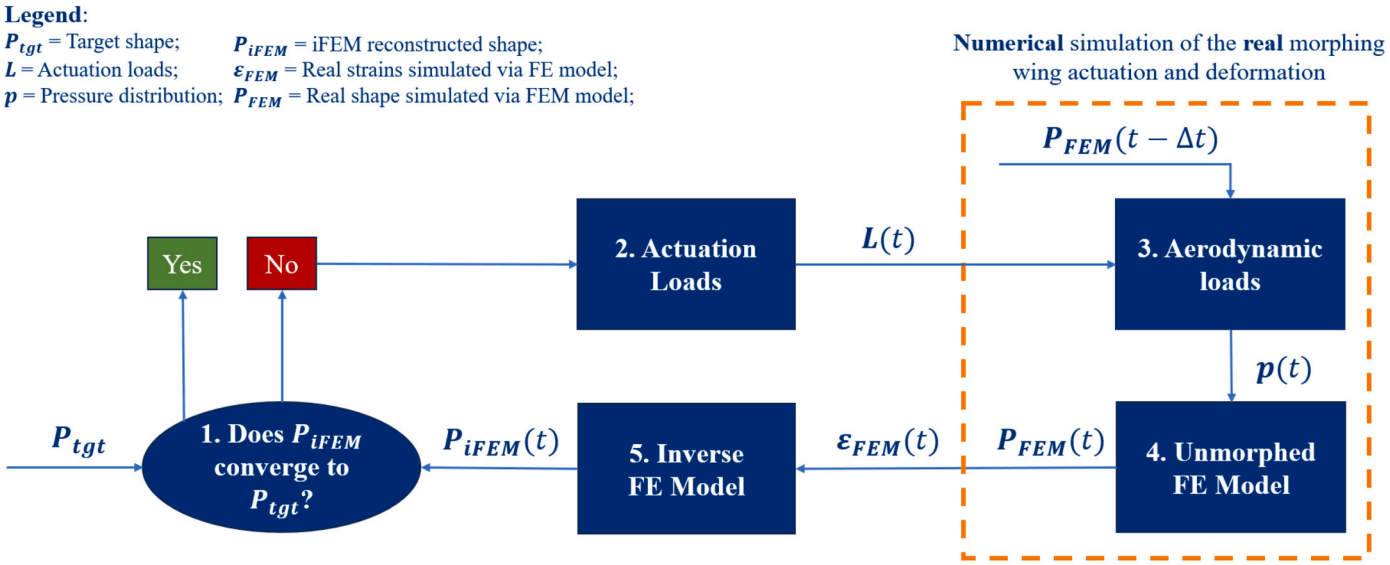


**Fig. 5.** Closed-loop control architecture.

$$\mathbf{P}=\begin{bmatrix} u_{X,1} & u_{Y,1} & u_{Z,1} \\ \vdots & \vdots & \vdots \\ u_{X,N_{n,s}} & u_{Y,N_{n,s}} & u_{Z,N_{n,s}} \end{bmatrix} \tag{1}$$

As mentioned in subsection 2.2, the FE model is used in the closed-loop control tests to simulate the experimental strains required for the iFEM feedback-based control strategy. In particular, it is assumed that, at the centroid of each element of the FE model, the in-plane strains are known (a detailed explanation of sensor placement is provided in subsection 4.2). Hence, the strains are collected in the form of a $N_{e,s}\times 6$ matrix as

$$\boldsymbol{\varepsilon}=\begin{bmatrix} \varepsilon^{+}_{xx,1} & \varepsilon^{-}_{xx,1} & \varepsilon^{+}_{yy,1} & \varepsilon^{-}_{yy,1} & \gamma^{+}_{xy,1} & \gamma^{-}_{xy,1} \\ \vdots & \vdots & \vdots & \vdots & \vdots & \vdots \\ \varepsilon^{+}_{xx,N_{e,s}} & \varepsilon^{-}_{xx,N_{e,s}} & \varepsilon^{+}_{yy,N_{e,s}} & \varepsilon^{-}_{yy,N_{e,s}} & \gamma^{+}_{xy,N_{e,s}} & \gamma^{-}_{xy,N_{e,s}} \end{bmatrix} \tag{2}$$

where $(\varepsilon^{+}_{xx},\varepsilon^{+}_{yy},\gamma^{+}_{xy})_i$ and $(\varepsilon^{-}_{xx},\varepsilon^{-}_{yy},\gamma^{-}_{xy})_i$ are respectively the top and bottom in-plane strains, measured in the local reference system of the i-th element, at its centroid.

Moving to the notation of the actuation load schemes, for the model using a set of $N_L$ sparse concentrated transverse forces, shown in Fig. 3, the magnitude of the loads is contained in a column vector, $\mathbf{L}$, defined as

$$\mathbf{L}=\{L_1,\cdots,L_{N_L}\}^T \tag{3}$$

Likewise, when the distributed pressure actuation scheme is used (Fig. 4), the load vector $\mathbf{L}$ contains the $N_{e,s}$ values of the pressure loads applied to the elements of the upper and lower skin surfaces.

Lastly, the time instant $t$, corresponding to the generic closed-loop iteration, is used to represent the variables produced during that iteration, while $t-\Delta t$ represents the variables computed in the previous iteration, assuming a time interval $\Delta t$ in between.

### 3.2. Control loop flowchart

The flowchart of the iFEM feedback-based closed-loop control strategy is presented in Fig. 5.

The closed-loop control architecture can be divided into 5 different stages:

1. In the first stage, the difference between the target and iFEM reconstructed displacements, referred to as $\mathbf{P}_{\mathbf{tgt}}$ and $\mathbf{P}_{\mathbf{iFEM}}(t)$ is calculated;
2. Then, in the second stage, this difference is used to compute the actuation loads, $\mathbf{L}(t)$;
3. In the third stage, the effect of external environmental loads on the morphing structure is introduced. For the present problem, this takes the form of the aerodynamic pressure distribution, $\mathbf{p}(t)$, over the upper and lower surface of the morphing wing;
4. The actuation loads and the aerodynamic pressure distribution are both fed, in the fourth stage, to the FE model of the unmorphed structure to produce a numerical simulation of the real wing deformations, $\mathbf{P}_{\mathbf{FEM}}(t)$, and of the real surface strains, $\boldsymbol{\varepsilon}_{\boldsymbol{FEM}}(t)$;
5. Lastly, in the fifth stage, the FEM simulated strains are used as the input for the iFEM analysis to produce the iFEM reconstructed shape, $\mathbf{P}_{\mathbf{iFEM}}(t)$, which is used as feedback for the controller, thus completing the closed-loop cycle.

As mentioned in subsection 2.1, morphing is exploited only to modify the camber of the trailing edge. Therefore, since the wing changes its shape predominantly in the transverse direction, the error used to verify convergence is defined using only the transverse distance between the top and bottom skin curves of the current and target morphed shape. While the current morphed shape is obtained using the iFEM analysis, the 'target curves' are computed by spline interpolation, using a certain number of points of the target morphed shape, that is

$$\begin{aligned} &spline(\mathbf{X}_{\mathbf{tgt}},\mathbf{Y}_{\mathbf{tgt}})\Rightarrow f(\mathbf{X}) \\ &\mathbf{Y}^{*}_{\mathbf{tgt}}=f(\mathbf{X}_{\mathbf{iFEM}}) \end{aligned} \tag{4}$$

where $\mathbf{X}_{\mathbf{tgt}}$ and $\mathbf{Y}_{\mathbf{tgt}}$ are vectors containing the global coordinates of the target shape. Eqn. (4) describes a continuous piece-wise polynomial interpolation (referred to as $spline(\mathbf{X}_{\mathbf{tgt}},\mathbf{Y}_{\mathbf{tgt}})$) that produces a curve function, $f(\mathbf{X})$, that is then evaluated in $\mathbf{X}_{\mathbf{iFEM}}$, the vector of global X-coordinates of the iFEM reconstructed shape. In other words, this procedure allows to slightly modify the set of points that define the target shape profile, from the original coordinates $(\mathbf{X}_{\mathbf{tgt}},\mathbf{Y}_{\mathbf{tgt}})$, to a set of points with coordinates $(\mathbf{X}_{\mathbf{iFEM}},\mathbf{Y}^{*}_{\mathbf{tgt}})$. This procedure allows to define a target shape whose nodes share the same X-coordinates with the nodes of the iFEM reconstructed shape. Thus, the convergence criterion is based on an error containing only the difference between the global Y-coordinates

of the nodes. In particular, the error is computed in the first stage of the closed-loop iterations following a least-squares approach, leading to the following expression

$$err_{\Delta Y}(t) = \sqrt{\frac{1}{N_{n,s}} \frac{\sum_{j=1}^{N_{n,s}} (Y^*_{j,tgt} - Y_{j,iFEM}(t))^2}{\max((\mathbf{Y}^*_{\mathbf{tgt}})^2)}} \tag{5}$$

where the variable $t$, as mentioned in the previous subsection, represents the time instant corresponding to the iteration in which the error is computed.

In the second stage, the procedure through which $\mathbf{P_{tgt}} - \mathbf{P_{iFEM}}(t)$ is used to compute the actuation load vector, $\mathbf{L}(t)$, is the one introduced by Roy et al. [31], which is based on the simplifying assumption that the structure experiences only linear deformations, thus the principles of linear analysis are employed. In particular, the difference $\mathbf{P_{tgt}} - \mathbf{P_{iFEM}}(t)$ produces the required displacements that the structure needs to achieve the target shape

$$\mathbf{D_{req}}(t) = \mathbf{P_{tgt}} - \mathbf{P_{iFEM}}(t) \tag{6}$$

where the letter **D** is used because, in contrast to the displacement matrix **P**, the required displacements are not measured with respect to the unmorphed shape. To compute the loads that produce $\mathbf{D_{req}}(t)$, a relation between the actuation scheme and the displacements is introduced following these steps: the FE model of the unmorphed structure is used to compute the nodal displacement matrices, $\mathbf{\Pi_m}$, representing the nodal displacements due to a unit load at the m-th actuation point of the morphing scheme. Each matrix $\mathbf{\Pi_m}$ can be rearranged as a column vector of the form

$$\mathbf{\Pi_m} = \{u_{X,1}, u_{Y,1}, u_{Z,1}, ..., u_{X,N_{n,s}}, u_{Y,N_{n,s}}, u_{Z,N_{n,s}}\}^T_m \quad m = 1, ..., N_L \tag{7}$$

Assembling all the $\mathbf{\Pi_m}$ column vectors in a single matrix, the matrix of influence coefficients, **C** is obtained:

$$\mathbf{C} = \left[\{\Pi_1\} \cdots \{\Pi_{N_L}\}\right] \tag{8}$$

The matrix of influence coefficients is a $3N_{n,s} \times N_L$ matrix (or a $3N_{n,s} \times N_{e,s}$ matrix for the distributed pressure actuation scheme). For a given actuation scheme, and for any set of values of the actuation loads represented by the load vector **L**, the correlated displacements are obtained via this simple equation:

$$\mathbf{P} = \mathbf{CL} \tag{9}$$

The **P** matrix obtained in Eqn. (9), as explained previously in subsection 3.1, contains the displacements computed with respect to the unmorphed shape. However, the function that computes the loads uses as input the difference between two **P** matrices, the one related to the target shape and the one obtained via the iFEM reconstruction. The equation that relates the matrix of influence coefficients to the difference between the two displacement matrices, $\mathbf{P_{tgt}}$ and $\mathbf{P_{iFEM}}(t)$ is

$$\mathbf{D}(t) = \mathbf{P_{tgt}} - \mathbf{P_{iFEM}}(t) = \mathbf{CL_{tgt}} - \mathbf{CL_{iFEM}}(t) = \mathbf{C\Delta L}(t) \tag{10}$$

where $\mathbf{\Delta L}(t)$ is used to represent the unknown load increment at the iteration corresponding to the generic time instant $t$.

At each iteration, Eqn. (10), together with the required displacement $\mathbf{D_{req}}(t)$, allows to build the least-squares difference functional

$$\Psi(\mathbf{\Delta L}(t)) = \left\| \mathbf{D_{req}}(t) - \mathbf{D}(t) \right\|^2 = \left\| \mathbf{D_{req}}(t) - \mathbf{C\Delta L}(t) \right\|^2 \tag{11}$$

Minimizing Eqn. (11) leads to the following least-squares problem:

$$\min_{\mathbf{\Delta L}(t)} \left\| \mathbf{D_{req}}(t) - \mathbf{C\Delta L}(t) \right\|^2 \tag{12}$$

Since the only independent variable of the least-squares functional is the unknown load increment, $\mathbf{\Delta L}(t)$, the solution of Eqn. (12) is exactly $\mathbf{\Delta L}(t)$ and can be obtained, for instance, using the singular value decomposition (SVD) of the matrix **C**. In particular, using the pseudo-inverse matrix $\mathbf{C}^\dagger$ [68], the load increment is computed as:

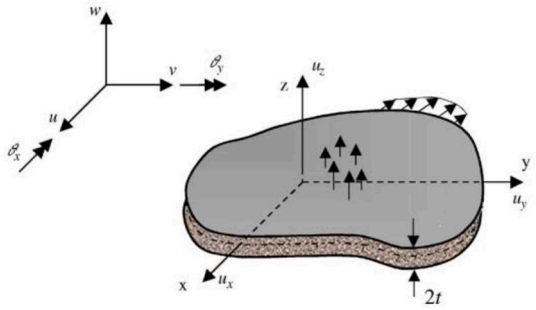


**Fig. 6.** Notation for the flat shell [44].

$$\mathbf{\Delta L}(t) = \mathbf{C}^\dagger \mathbf{D_{req}}(t) \tag{13}$$

$\mathbf{\Delta L}(t)$, however, is not the final output of the process yet. $\mathbf{L}(t)$, the actuation load vector that, as shown in 5, is the actual controller output, and that is used as an input for the FEM procedure, is obtained at the time instant t with the following expression:

$$\mathbf{L}(t) = \mathbf{L}(t - \Delta t) + \mathbf{\Delta L}(t) \tag{14}$$

In the third stage, the aerodynamic pressure distribution is computed by feeding the deformed FEM simulated shape computed at the previous iteration, $\mathbf{P_{FEM}}(t - \Delta t)$, to XFOIL [69], which produces the pressure distribution on the morphed profile. In particular, to simplify the procedure, the analysis are run under a laminar flow regime. Moreover, it is assumed that the pressure distribution is constant along the span. Thus, only the deformed shape of a reference section, at mid-span, is extracted from $\mathbf{P_{FEM}}(t - \Delta t)$ and fed to XFOIL.

Lastly, as introduced at the beginning of this subsection, the fourth and fifth stages consist of the direct FEM and inverse FEM analysis. In particular, as the fifth stage represents the core of the present effort, the following Section is entirely dedicated to the in-detail explanation of the iFEM theory and the model used for the iFEM analysis.

## 4. The inverse Finite Element Method

Before presenting the results, this Section aims to briefly introduce the shape sensing method known as the inverse Finite Element Method and its underlying theory, as well as the iFEM model used for the morphing wing.

### 4.1. The iFEM framework

Shape sensing is defined as the inverse problem of reconstructing the deformed shape of a structure using surface strain measurements. In the inverse Finite Element Method, the strain measurements are used to build a least-squares error functional, Φ. Minimizing this functional yields Euler equations and consistent boundary conditions that relate the measured strains to the unknown displacement field [44]. In other words, iFEM is a least-squares variational principle based method.

The structural framework model for the inverse Finite Element Method applied to thin-walled structures is the First-order Shear Deformation Theory (FSDT or Mindlin theory). With reference to Fig. 6, the FSDT displacement field is defined as

$$\begin{aligned} u_x(x,y,z) &= u(x,y) + z\theta_y(x,y) \\ u_y(x,y,z) &= v(x,y) + z\theta_x(x,y) \\ u_z(x,y,z) &= w(x,y) \end{aligned} \tag{15}$$

where $\mathbf{u} = \{u, v, w, \theta_x, \theta_y\}^T$ is the vector of the five kinematic variables, which all refer to displacements and bending rotations defined on the middle plane of the shell structure. The kinematic model of Eqs. (15) leads to the following expression for the in-plane strains:

$$\begin{Bmatrix} \varepsilon_{xx} \\ \varepsilon_{yy} \\ \gamma_{xy} \end{Bmatrix} = \begin{Bmatrix} \varepsilon_{x0} \\ \varepsilon_{y0} \\ \gamma_{xy0} \end{Bmatrix} + z \begin{Bmatrix} \kappa_{x0} \\ \kappa_{y0} \\ \kappa_{xy0} \end{Bmatrix} \equiv \mathbf{e}(\mathbf{u}) + z\mathbf{k}(\mathbf{u}) \tag{16}$$

where **e(u)** is the vector of membrane strains, and **k(u)** the vector of curvatures. Both vectors are related to the five kinematic variables by $3 \times 5$ differential operator matrices:

$$\begin{aligned} \mathbf{e}(\mathbf{u}) &= \mathbf{L}_\varepsilon \mathbf{u} \\ \mathbf{k}(\mathbf{u}) &= \mathbf{L}_\kappa \mathbf{u} \end{aligned} \tag{17}$$

Similarly, transverse shear strains are related to $\mathbf{u}$ via a $2 \times 5$ differential operator matrix:

$$\begin{Bmatrix} \gamma_{xz} \\ \gamma_{yz} \end{Bmatrix} \equiv \begin{Bmatrix} \gamma_{xz0} \\ \gamma_{yz0} \end{Bmatrix} \equiv \mathbf{g}(\mathbf{u}) = \mathbf{L}_\gamma \mathbf{u} \tag{18}$$

The membrane strains, $\mathbf{e}$, together with the bending curvatures, $\mathbf{k}$, and the transverse shear strains, $\mathbf{g}$, are defined as analytical strain measures.

According to the well-established finite element approximation strategy, the thin-walled structure is discretized using (inverse) finite elements. Within each of these inverse elements, $\mathbf{u}$ is expressed as a function of $\mathbf{u^e}$, the nodal displacement vector:

$$\mathbf{u}(x, y) = \mathbf{N}(x, y)\mathbf{u^e} \tag{19}$$

where $\mathbf{N}$ is a matrix containing appropriate shape functions.

Introducing Eqn. (19) in Eqs. (17) and (18), the analytical strain measures can be expressed as functions of the nodal displacements:

$$\begin{aligned} \mathbf{e}(\mathbf{u^e}) &= \mathbf{L}_\varepsilon \mathbf{N}\mathbf{u^e} = \mathbf{B^m}\mathbf{u^e} \\ \mathbf{k}(\mathbf{u^e}) &= \mathbf{L}_\kappa \mathbf{N}\mathbf{u^e} = \mathbf{B^b}\mathbf{u^e} \\ \mathbf{g}(\mathbf{u^e}) &= \mathbf{L}_\gamma \mathbf{u^e} = \mathbf{B^s}\mathbf{u^e} \end{aligned} \tag{20}$$

where $\mathbf{B^m}$, $\mathbf{B^b}$, and $\mathbf{B^s}$ are matrices of shape function derivatives corresponding to the membrane, bending, and transverse shear strain measures, respectively [70].

The iFEM least-squares functional, $\Phi$, is built using the surface strain measurements. However, in order to employ the strain measurements in the definition of $\Phi$, they have to be first expressed in terms of membrane strains and curvatures. Referring to the notation of Fig. 6, let the position of the i-th strain sensor pair (for instance, a couple of FBG sensors or strain rosettes) on the top or bottom surface of the plate be $\mathbf{x_i} = (x_i, y_i, \pm t)$. The strains measured by the sensor on the top-skin are $(\varepsilon^+_{xx}, \varepsilon^+_{yy}, \gamma^+_{xy})_i$, whereas the strains measured on the bottom are $(\varepsilon^-_{xx}, \varepsilon^-_{yy}, \gamma^-_{xy})_i$. Having sensors on both the top and bottom surface, the strain measurements can be converted into experimentally evaluated membrane strains and curvatures using the following equations:

$$\mathbf{e}^\varepsilon_\mathbf{i} \equiv \begin{Bmatrix} \varepsilon^\varepsilon_{x0} \\ \varepsilon^\varepsilon_{y0} \\ \gamma^\varepsilon_{xy0} \end{Bmatrix}_i = \frac{1}{2}\left( \begin{Bmatrix} \varepsilon^+_{xx} \\ \varepsilon^+_{yy} \\ \gamma^+_{xy} \end{Bmatrix}_i + \begin{Bmatrix} \varepsilon^-_{xx} \\ \varepsilon^-_{yy} \\ \gamma^-_{xy} \end{Bmatrix}_i \right), \qquad (i = 1, ..., n) \tag{21}$$

$$\mathbf{k}^\varepsilon_\mathbf{i} \equiv \begin{Bmatrix} \kappa^\varepsilon_{x0} \\ \kappa^\varepsilon_{y0} \\ \kappa^\varepsilon_{xy0} \end{Bmatrix}_i = \frac{1}{2t}\left( \begin{Bmatrix} \varepsilon^+_{xx} \\ \varepsilon^+_{yy} \\ \gamma^+_{xy} \end{Bmatrix}_i - \begin{Bmatrix} \varepsilon^-_{xx} \\ \varepsilon^-_{yy} \\ \gamma^-_{xy} \end{Bmatrix}_i \right), \qquad (i = 1, ..., n) \tag{22}$$

where $n$ is the number of sensors and the $i$ subscript stands for $\mathbf{x} = \mathbf{x_i}$.

The experimentally evaluated membrane strains and curvatures of Eqs. (21) and (22), together with the FSDT analytical strain measures of Eqs. (20) are used to formulate the least-squares error functional associated with the generic element $e$ of the iFEM discretization

$$\Phi^e(\mathbf{u^e}) = \mathbf{w_e} \left\| \mathbf{e}(\mathbf{u^e}) - \mathbf{e}^\varepsilon \right\|^2 + \mathbf{w_k} \left\| \mathbf{k}(\mathbf{u^e}) - \mathbf{k}^\varepsilon \right\|^2 + \mathbf{w_g} \left\| \mathbf{g}(\mathbf{u^e}) - \mathbf{g}^\varepsilon \right\|^2 \tag{23}$$

In Eqn. (23), $\mathbf{w_e}$, $\mathbf{w_k}$, and $\mathbf{w_g}$ represent the row vectors of weighting coefficients related, respectively, to the membrane, the curvature, and the transverse shear strain measures. The weighting coefficients control the degree of enforcement between the analytical and the experimentally evaluated strain measures, i.e., the degree of enforcement of the following relations:

$$\begin{aligned} &\mathbf{e}(\mathbf{u^e}) \to \mathbf{e}^\varepsilon \\ &\mathbf{k}(\mathbf{u^e}) \to \mathbf{k}^\varepsilon \\ &\mathbf{g}(\mathbf{u^e}) \to \mathbf{g}^\varepsilon \end{aligned} \tag{24}$$

A strong enforcement of Eqs. (24) is obtained by setting the weighting coefficients to one and it can be applied when the measured strains are known. This is the case of the experimentally evaluated membrane and curvature strain measures, $\mathbf{e}^\varepsilon$ and $\mathbf{k}^\varepsilon$, that can be directly obtained from the experimental strain measurements using Eqs. (21) and (22). Accordingly, the norms of Eqn. (23), are calculated using the following expressions:

$$\begin{aligned} \left\| \mathbf{e}(\mathbf{u^e}) - \mathbf{e}^\varepsilon \right\|^2 &\equiv \frac{1}{A^e} \int_{A^e} \left[ \mathbf{e}(\mathbf{u^e}) - \mathbf{e}^\varepsilon \right]^2 \mathrm{d}A^e \\ \left\| \mathbf{k}(\mathbf{u^e}) - \mathbf{k}^\varepsilon \right\|^2 &\equiv \frac{(2t)^2}{A^e} \int_{A^e} \left[ \mathbf{k}(\mathbf{u^e}) - \mathbf{k}^\varepsilon \right]^2 \mathrm{d}A^e \end{aligned} \tag{25}$$

where $A^e$ is the area of the inverse element.

On the other hand, if the strain measures can not be experimentally evaluated, the corresponding weighting coefficients are set to a small value, for instance, $10^{-4}$. This always applies to the experimentally evaluated transverse shear strain measures, $\mathbf{g}^\varepsilon$, as they cannot be obtained directly from the strain measurements. Consequently, the corresponding norm of Eqn. (23) is computed as

$$\left\| \mathbf{g}(\mathbf{u^e}) - \mathbf{g}^\varepsilon \right\|^2 \equiv \int_{A^e} \mathbf{g}(\mathbf{u^e})^2 \, \mathrm{d}A^e \tag{26}$$

A similar definition of the norms (instead of those in Eqs. (25)), and small values of the corresponding weighting coefficients are used for membrane and curvature strain measures within those elements where no experimental evaluations are available.

From the explicit expression of the squared norms of Eqs. (25) and (26), it is evident that the inverse element least-squares functional, $\Phi^e(\mathbf{u^e})$, depends only on the element nodal displacements. Therefore, minimizing the element functional leads to the following problem:

$$\frac{\partial \Phi^e(\mathbf{u^e})}{\partial \mathbf{u^e}} = \mathbf{K^e}\mathbf{u^e} - \mathbf{f^e} = 0 \implies \mathbf{K^e}\mathbf{u^e} = \mathbf{f^e} \tag{27}$$

which is the element matrix equation, where $\mathbf{K^e}$ is a function of the positions of the strain sensors, as is the vector $\mathbf{f^e}$, which also depends on the measured strain data. Through appropriate rotations of the element vectors and coefficient matrices, and using finite element assembling techniques, the iFEM produces a system of algebraic equations for the whole structure

$$\mathbf{KU} = \mathbf{F} \tag{28}$$

whose solution yields the nodal displacements of the structure.

To obtain a non-singular coefficient matrix, boundary conditions are to be imposed. On the contrary, to solve for the displacements of the structure, elastic or inertial material properties can be unknown. This constitutes a key advantage of the iFEM procedure together with its potential to be applied to both static and dynamic systems. Furthermore, in applications where the strain sensor's position is fixed and the only variables are the measured strain data, the iFEM analysis has a low computational cost, since the analysis themselves require only the calculation of $\mathbf{F}$, while $\mathbf{K}$ remains constant. These advantages make the

iFEM applicable and effective in real-time case scenarios, such as the control strategy of the morphing wing structure.

### 4.2. The iFEM model

For the iFEM analysis, the inverse finite element model of the morphing wing structure is built using 2D inverse four-node quadrilateral elements, the iQS4 [45]. These elements have 6 DOF (degrees of freedom) at each node and employ $C^0$-continuous anisoparametric shape functions (interested readers may refer to [45] for the expressions of the shape functions). In particular, the inverse model consists solely of iQS4 elements, so that the iFEM mesh is the same as the 2D FEM mesh used to model the skin, and that is represented in black in Fig. 3. The reason is that the iFEM feedback is used to monitor only the external shape of the structure, which can be obtained by simply reconstructing the displacements of the skin.

To accomplish this iFEM shape reconstruction, as explained in the previous subsection, the measured strains are paramount. To simulate them, it is assumed that every element of the skin, and thus of the FEM and, notably, the iFEM mesh, is instrumented with a strain rosette on both its top and bottom surfaces. In reality, it would be very difficult to have strain sensors on the inner interface between the skin and the foam core (integrated Fiber Bragg Grading sensors should be used). Nevertheless, to validate the procedure, the assumption is made that this measurement is possible so that the back-to-back tri-axial strains at all the element centroids are known. This assumption allows for a full-field (i.e. at every material point) reconstruction of the displacements.

## 5. Results

This Section contains the main numerical results of the closed-loop architecture. Parametric analyses were carried out to draw comparative results. Three test parameters were considered:

- the actuation scheme employed;
- the target shape;
- the intensity of the aerodynamic pressure distribution acting on the structure, which was controlled by the value of the velocity, $V$, as the aerodynamic pressure is defined by the following expression:

$$\mathbf{p} = \frac{1}{2}\rho V^2 \mathbf{c_p} \tag{29}$$

where $\rho = 1.225$ kg/m$^3$ is the density of the air, and $\mathbf{c_p}$ is the vector of the pressure coefficients.

The results are presented in terms of the transverse relative least-squares error, $err_{\Delta Y}$ (see Eqn. (5)), plotted against the number of iterations. In addition to the line plots, the 3D iFEM reconstructed shape plots are also shown: each plot is colored to represent the distribution of the nodal transverse relative error:

$$\delta Y_j = \frac{|Y^*_{j,tgt} - Y_{j,iFEM}|}{max(|\mathbf{Y^*_{tgt}}|)} \tag{30}$$

which, excluding the normalizing factor $1/\sqrt{N_{n,s}}$, is the j-th term of the summation of Eqn. (5).

Before introducing the results, the target shapes employed and their definition are presented.

### 5.1. Target shapes

As explained in Section 1, the morphing capabilities of the chosen wing design are exploited only to modify the camber of the trailing edge of the wing itself. For a NACA airfoil, such as the one used for the wing profile, camber morphing can be achieved by modifying just the equation of the camber line, as the equation of both the top and bottom skin change accordingly. In particular, for the results presented in this Section, the camber line equation is modified so that it morphs into an arbitrary parabolic shape. This leads to the following expression of the transverse global coordinate of the camber line:

$$Y_{c,tgt}(x) = Y_{c0} - k \cdot (X - X_m)^2 \tag{31}$$

where the term $Y_{c0}$ is used to guarantee the continuity of the equation with the unmorphed portion of the wing and $X_m = 0.55$ is the coordinate along the chord of the front part of the morphing trailing edge. The term $k$ represents an arbitrary constant that is used to control the extent of the downward transverse deflection of the profile and that, from a practical perspective, could be understood as the variable used to maneuver the morphing trailing edge as a control surface. In the case studies presented in this Section, the value of the constant was set to $k = 0.4$ and $k = 1$. The target shapes obtained are shown in Fig. 7.

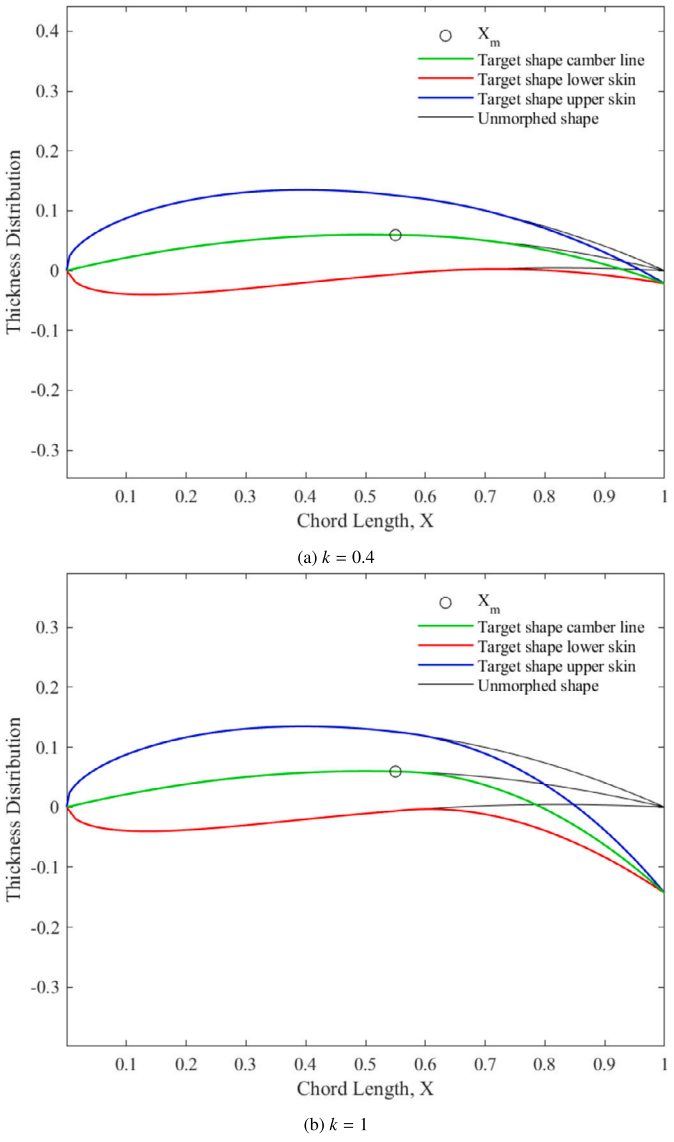


**Fig. 7.** Target shapes.

### 5.2. Parametric analysis: actuation scheme

The first test of the closed-loop architecture aims to evaluate the behavior of the control algorithm, comparing the case where the morphing trailing edge is actuated by transverse concentrated forces with the case where the distributed pressure is employed. Both actuation schemes

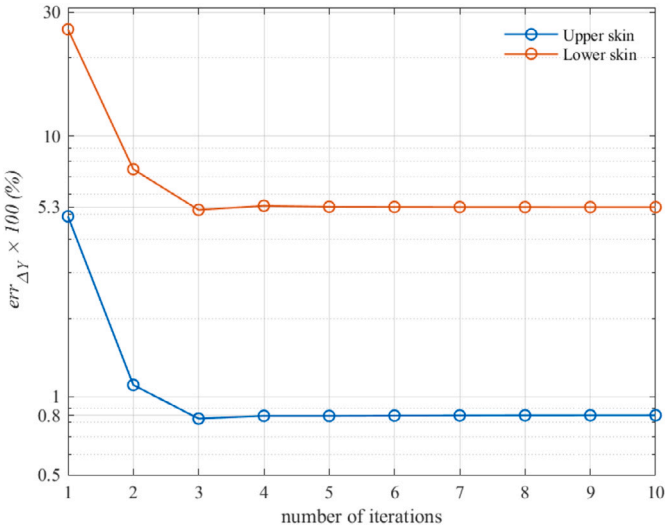


(a) Sparse transverse forces

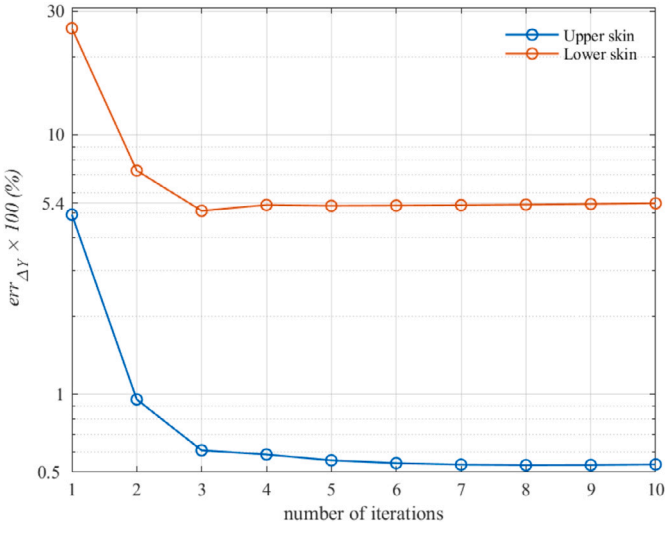


(b) Distributed pressure

**Fig. 8.** Comparison of closed-loop control architecture behavior with two different actuation schemes.

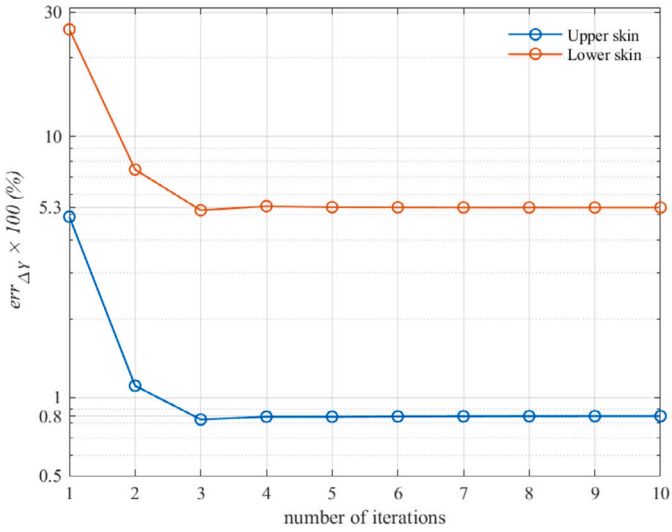


(a) $k = 0.4$

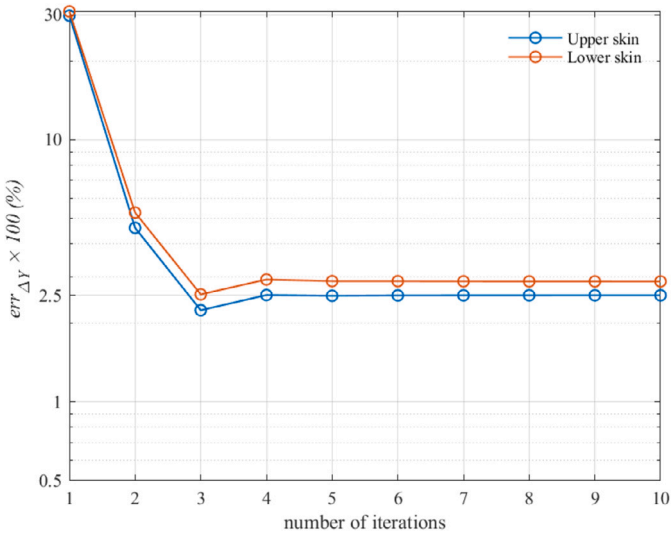


(b) $k = 1$

**Fig. 9.** Comparison of closed-loop control architecture behavior with two different target shapes.

were presented in subsection 2.2. The test is carried out considering the target shape obtained with $k = 0.4$ and a velocity $V = 0$ m/s, i.e., with no aerodynamic loads acting on the structure. The results are shown in Fig. 8, where the error is plotted against the number of iterations. Comparing the results obtained with the two actuation schemes, it is evident that, in both cases, the closed-loop strategy is able to rapidly converge to the target shape and with the same error values: less than 1% for the upper skin and around 5% for the lower skin. These results are confirmed by the colored 3D iFEM reconstructed shape plots, which show that, in the final iteration, the structure morphs to the target shape with a maximum value of the nodal transverse relative error, $\delta Y_j$, of 0.03. These plots are contained in Appendix A.

It can be concluded from these results that if no aerodynamic load acts on the structure, the iFEM feedback-based closed-loop control strategy is able to immediately converge to the target shape after the second iteration. Furthermore, different actuation schemes can be employed without affecting the behavior of the closed-loop architecture. Therefore, in the rest of this Section, only results obtained using the transverse concentrated forces actuation scheme are considered.

### 5.3. Parametric analysis: target shape

After testing the influence of the actuation scheme, the effect of a different target shape is addressed: the target shapes obtained using $k = 0.4$ and $k = 1$ are chosen. The tests are run setting a velocity $V = 0$ m/s and, as mentioned previously, employing only the transverse concentrated forces actuation scheme.

In Fig. 9, the error trends for the two case studies are compared: the different target shapes minimally affect the closed-loop iterations as, although in both cases the control algorithm rapidly converges to the target shape, the end error values are slightly different. However, looking at the 3D colored plots of Fig. B.1, which show the nodal transverse relative error, $\delta Y_j$, all over the morphed structure in the final iteration, it is evident that, in both cases, the closed-loop strategy is able to converge to the target shape. The slight difference in the error values of Fig. 9 is caused only by a small misalignment between the final morphed shape and the target shape at the rear end of the trailing edge in the case where $k = 1$, which can be observed in Fig. B.1b.

Therefore, as for the actuation scheme, the different target shapes do not impact the iFEM feedback-based closed-loop control over the mor-

phing trailing edge. Thus, in the following subsection, only the target shape obtained with $k = 0.4$ is considered.

### 5.4. Parametric analysis: aerodynamic pressure intensity

The previous results were obtained assuming $V = 0$ m/s, i.e., the aerodynamic pressure distribution on the structure is null. This last subsection is dedicated to the investigation of the effect of such external action on the iFEM feedback-based controller. As for the previous subsections, a parametric analysis is carried out, setting $k = 0.4$ for the target shape, the transverse concentrated forces as the actuation scheme, and varying the airflow velocity. Three different values are considered: $V = 100$ m/s, $V = 200$ m/s, and $V = 300$ m/s.

The results for $V = 100$ m/s are presented in Fig. 10a, where the transverse least-squares relative error, $err_{\Delta Y}$, is plotted against the number of iterations.

Comparing the graph of Fig. 10a with the one Fig. 8a, the aerodynamic pressure distribution has little to no effect on the structure and the controller is able to converge to the error values of around 5% for the lower skin and 0.8% for the upper skin. Similarly, the barely noticeable effect of the pressure distribution can be observed comparing Fig. C.1a and Fig. C.3a: the controller achieves the target shape on the second iteration, and the distribution of nodal transverse relative error, $\delta Y_j$, remains almost identical between the second and the last iteration, with its maximum staying around the value of 0.03.

To see a noticeable effect of the aerodynamic pressure distribution on the structure the velocity is increased to $V = 200$ m/s. The maximum pressure value, which was around 8000 Pa in the previous case study, now rises to 30000 Pa, as shown in Fig. C.2. Looking at the comparison of the 3D colored plots in the second closed-loop iteration, presented in Fig. C.1, the effects of the pressure distribution are much more visible, as it slows the convergence by slightly tilting the tip of the trailing edge in the upward direction. On the other hand, this increase of lifting action caused by the aerodynamic pressure does not create an evident change in the trend of the graph in Fig. 10b: the error converges once again to the same error values of around 5% the bottom surface and a value of less than 1% for the top one.

Conversely, when the velocity is augmented to $V = 300$ m/s, the disturbance creates a high amplitude oscillating pattern, as shown in Fig. 10c. The response of the structure is caused by the oscillations of the pressure distribution and its peaks, that, as shown in Fig. C.2, range now from 60000 to 80000 Pa. The results of these high-pressure peak values are also reflected in the 3D colored plots (see Fig. C.1c): in the second iteration the upward tilt of the morphing wing is far more noticeable, and the maximum value of the nodal transverse relative error, $\delta Y_j$, rises to 0.15. Nevertheless, even though it requires more than one hundred iterations, the controller is able to suppress the oscillations, converging to the target shape, and achieving the $err_{\Delta Y}$ values of around 5% and less than 1% for the lower and upper skin, respectively (Fig. 10c). Lastly, similarly to the previous cases, a maximum nodal transverse relative error of 0.04 (Fig. C.3c) is achieved.

## 6. Conclusions

The problem of developing and assessing a closed-loop strategy for the morphing of wing structures where the feedback comes from the global deformed structural shape has been addressed in this work. The investigation has been conducted numerically on a simple wing segment with a morphable trailing edge, actuated by concentrated forces or distributed pressures, and with aerodynamic loads updated while the morphing is occurring. The deformed shape of the trailing top and bottom skin is reconstructed by using the inverse Finite Element Method (iFEM), a FE-based numerical approach matching, in a least-square sense, the analytical strains and those “measured” in some discrete locations.

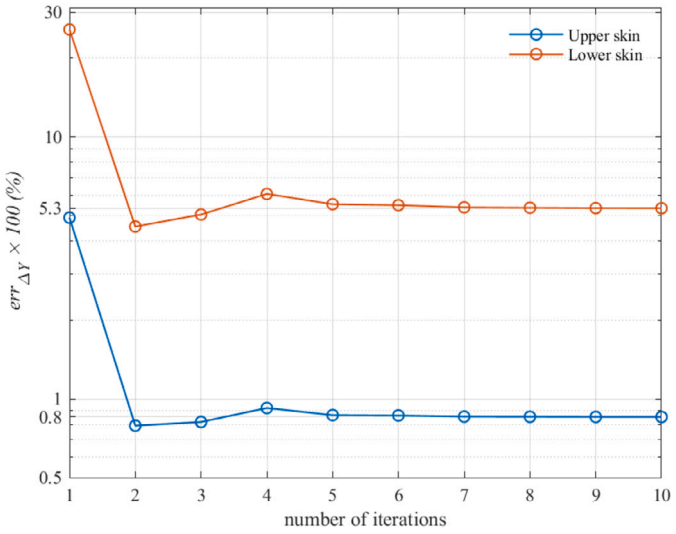


(a) $V = 100\ m/s$

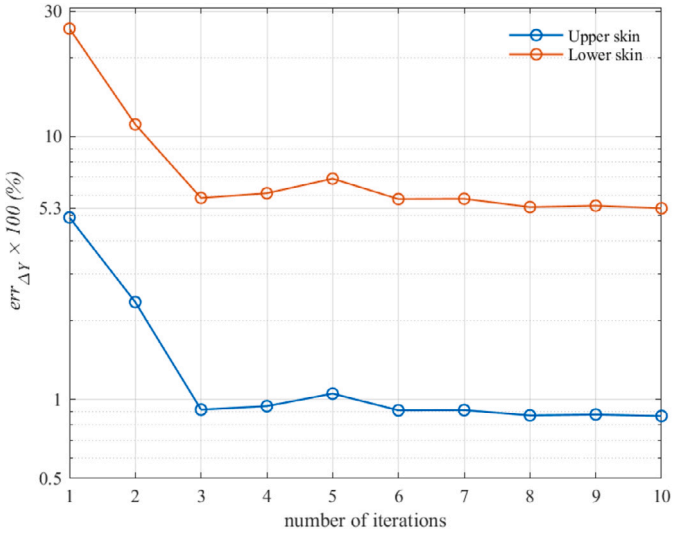


(b) $V = 200\ m/s$

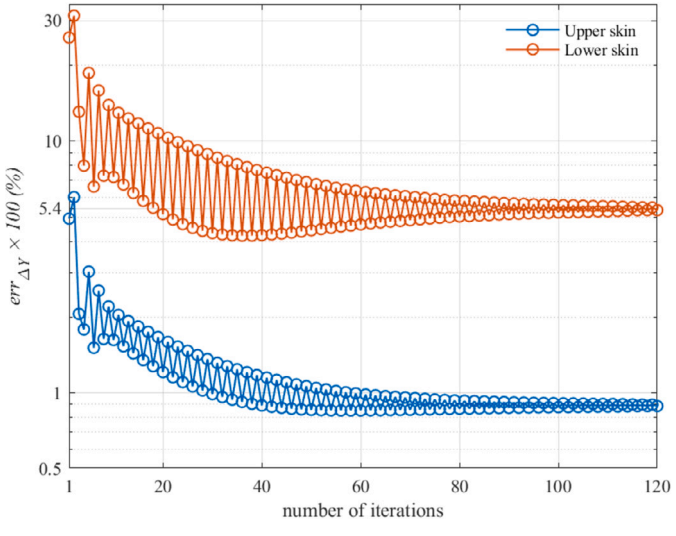


(c) $V = 300\ m/s$

**Fig. 10.** Comparison of the closed-loop control architecture behavior with three different intensity levels of the aerodynamic pressure distribution.

The closed-loop strategy is based on the target shape to achieve, on iFEM reconstructing the actual shape from some strain measurements, and on the actuation loads computed in order to correct the actual shape. The fundamentals of iFEM and of actuation loads evaluation are summarized in order to set the numerical framework for the investigation.

The assessment of the proposed control-loop strategy has been conducted on the FE model of the wing segment subjected to aerodynamic loads (computed via XFOIL) and actuation loads. The "measured" strains needed as input data for the iFEM-based feedback are evaluated on the trailing-edge skin. The morphing control assessed at different air-flow velocities demonstrated good performances in terms of convergence and accurate final trailing-edge shape. On the other hand, the proposed strategy employed a high number of sensor measurements and, in the harshest aerodynamic load conditions, required numerous iterations to suppress the structure's oscillations.

Future efforts of the ongoing research study will address further enhancements of the proposed strategy, including more realistic wing structures and actuation mechanisms, and more efficient actuation loads computation that reduces oscillations during the morphing process. Moreover, strategies to reduce the number of required strain sensors will be investigated, both using strain pre-extrapolation techniques and seeking optimal sensor configurations. Comparative investigations will be also performed where the performances of the proposed strategy are evaluated against those of existing approaches.

## CRediT authorship contribution statement

**Vincenzo Biscotti:** Writing – review & editing, Writing – original draft, Visualization, Validation, Software, Methodology, Investigation, Formal analysis, Data curation, Conceptualization. **Rinto Roy:** Writing – review & editing, Supervision, Software, Methodology, Conceptualization. **Marco Gherlone:** Writing – review & editing, Supervision, Methodology, Conceptualization.

## Declaration of competing interest

The authors declare that they have no known competing financial interests or personal relationships that could have appeared to influence the work reported in this paper.

## Acknowledgements

This research did not receive any specific grant from funding agencies in the public, commercial, or not-for-profit sectors.

## Appendix A. Actuation scheme comparison

In the figures of the appendices, the 3D iFEM reconstructed shapes are presented. The 3D plots are colored based on the values of the nodal transverse relative error, $\delta Y_j$ (see Eqn. (30)). The top and bottom views of the morphing trailing edge are shown to highlight the distribution of $\delta Y_j$ on the skin, whereas, in the lateral view, the difference between the iFEM reconstructed shape and the target shape, which is represented with black outlines, is clearly visible. In particular, in this appendix, the 3D colored plots of Fig. A1 and Fig. A2 help to draw the comparison between the behavior of the two actuation schemes tested (the concentrated forces and the distributed pressure), showing how they barely affect the control strategy.

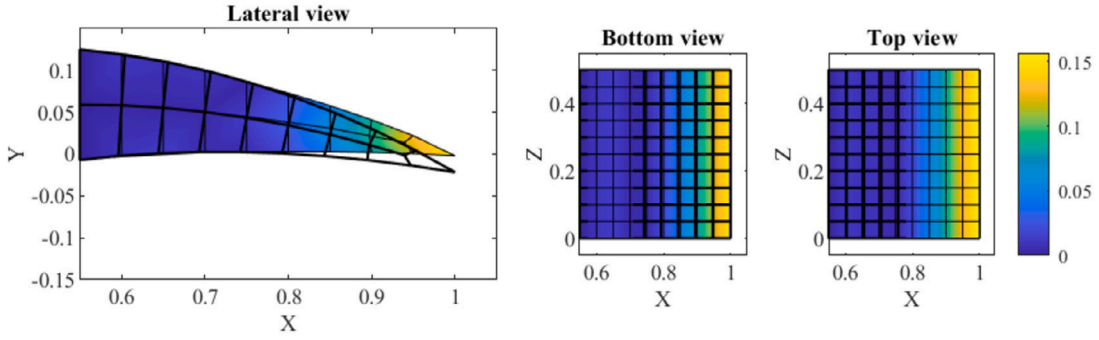


(a) First iteration

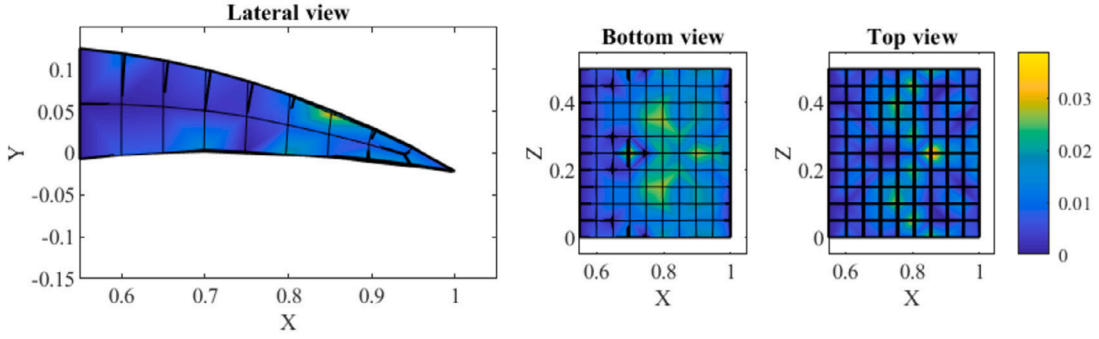


(b) Last iteration

**Fig. A1.** $\delta Y_j$ error plot on the iFEM reconstructed shape - $k = 0.4$, $V = 0$ m/s, sparse transverse forces actuation scheme.

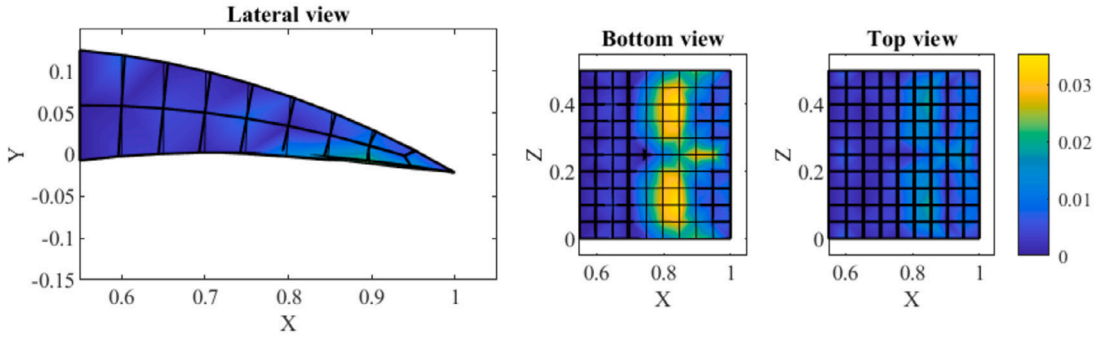


(a) Last iteration

**Fig. A2.** $\delta Y_j$ error plot on the iFEM reconstructed shape - $k = 0.4$, $V = 0$ m/s, distributed pressure actuation scheme.

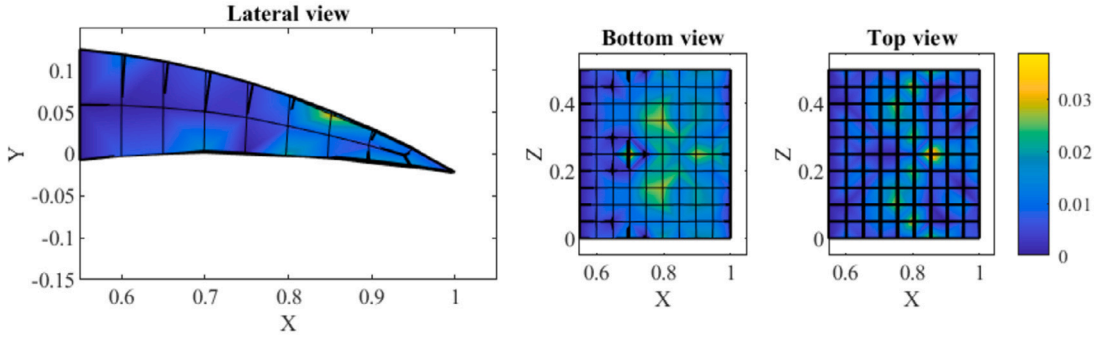


(a) $k = 0$

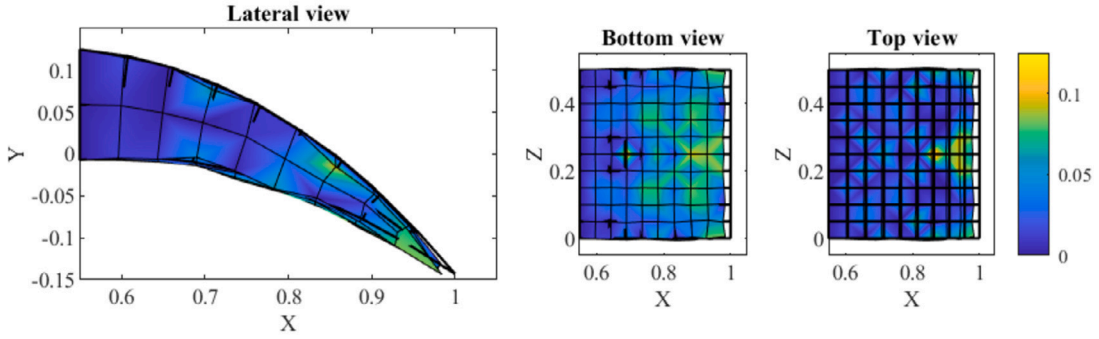


(b) $k = 1$

**Fig. B.1.** $\delta Y_j$ error plot on the iFEM reconstructed shape - $V = 0$ m/s - Last iteration.

## Appendix B. Target shape comparison

In this appendix, the 3D colored plots of Fig. B.1 are used to compare the behavior of the closed-loop control strategy when tested with two different target shapes. The results presented in Fig. B.1a show that, when $k = 0.4$, the control strategy converges to the target shape. On the other hand, the results of Fig. B.1b highlight a slight misalignment between the iFEM reconstructed shape and the target shape. However, as the nodal transverse error distributions are almost identical, it can be concluded that different target shapes barely affect the behavior of the control strategy.

## Appendix C. Pressure intensity comparison

The results presented in this appendix help to assess how the intensity of the aerodynamic pressure distribution varies with the relative wind speed, $V$, (see Fig. C.2) and, consequently, how the closed-loop it-

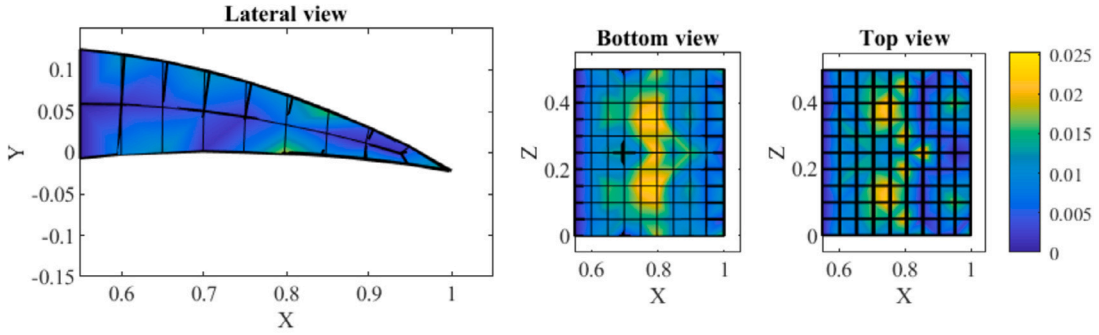


(a) $V = 100\ m/s$

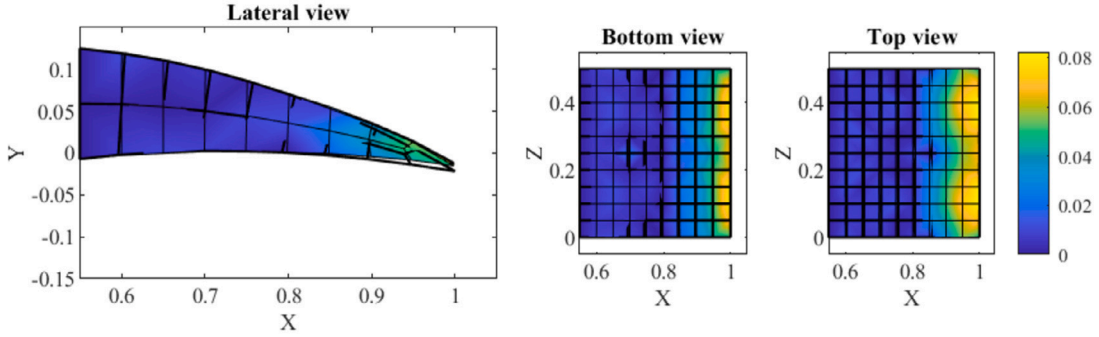


(b) $V = 200\ m/s$

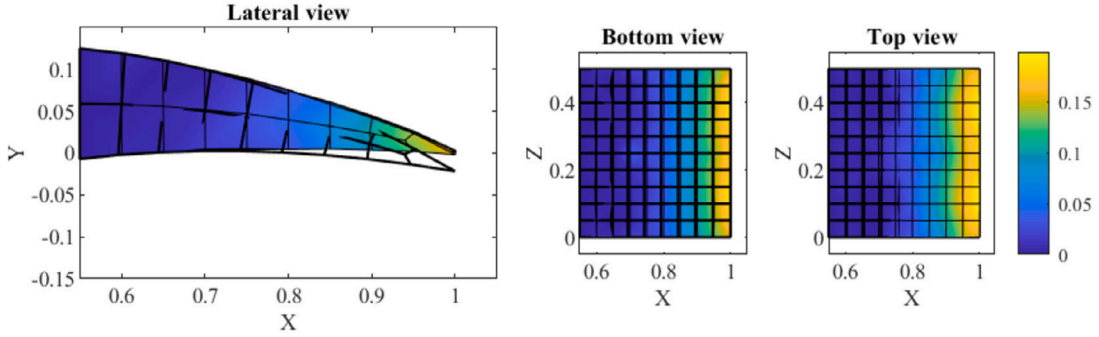


(c) $V = 300\ m/s$

**Fig. C.1.** $\delta Y_j$ error plot on the iFEM reconstructed shape - $k = 0.4$, sparse transverse forces actuation scheme - Second iteration.

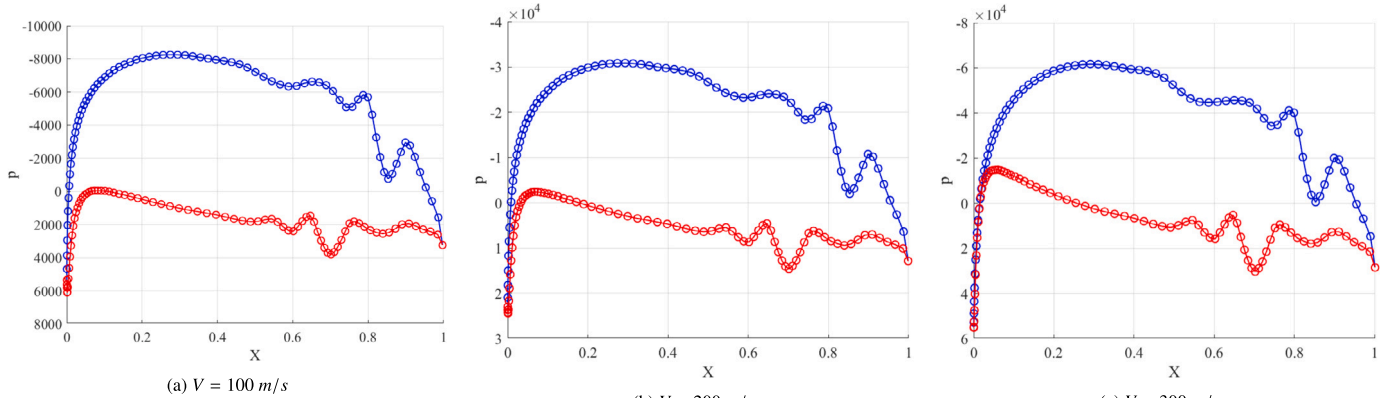


(a) $V = 100\ m/s$

(b) $V = 200\ m/s$

(c) $V = 300\ m/s$

**Fig. C.2.** Pressure distribution - $k = 0.4$, sparse transverse forces actuation scheme - Second iteration.

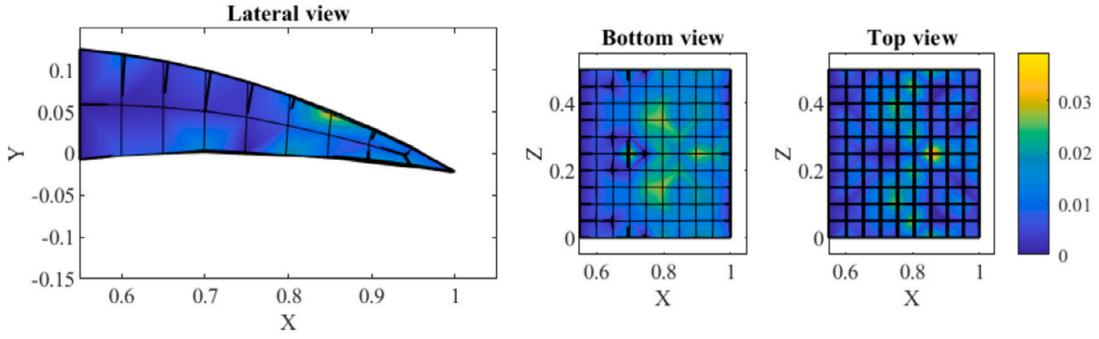


(a) $V = 100\ m/s$

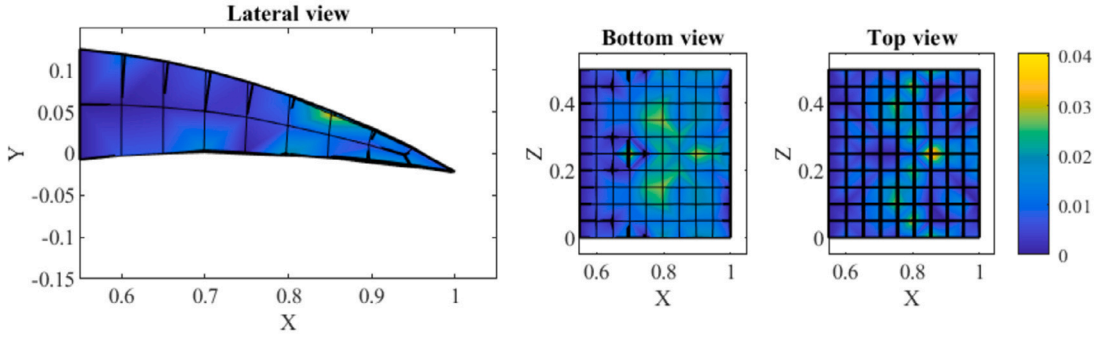


(b) $V = 200\ m/s$

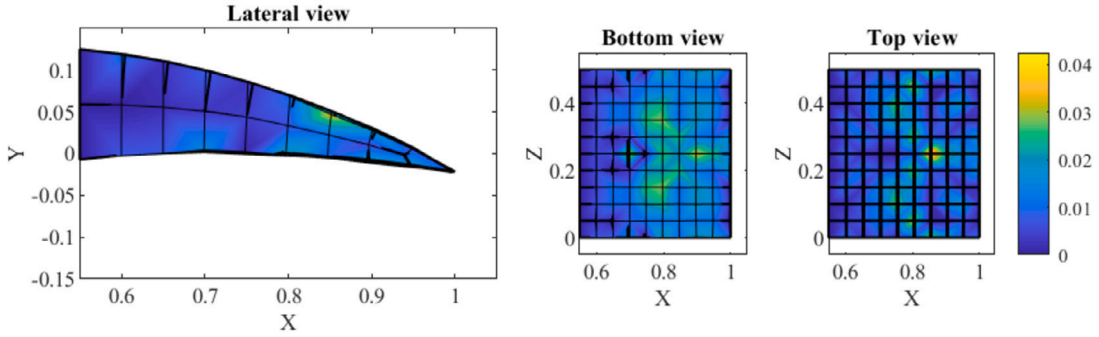


(c) $V = 300\ m/s$

**Fig. C.3.** $\delta Y_j$ error plot on the iFEM reconstructed shape - $k = 0.4$, sparse transverse forces actuation scheme - Last iteration.

erations are affected by this variable aerodynamic load (see Fig. C.1), Moreover, the results are used to confirm that, even when confronting the harshest aerodynamic pressure distribution, the controller is still able to converge to the target shape (see Fig. C.3).

## Data availability

Data will be made available on request.

## References

[1] © Cambridge University Press & Assessment 2024, Metamorphosis | meaning - Cambridge learner's dictionary. https://dictionary.cambridge.org/dictionary/learner-english/metamorphosis, 2024. [Accessed 8 December 2024].

[2] Sofla A, Meguid S, Tan K, Yeo W. Shape morphing of aircraft wing: status and challenges. Mater Des 2010;31(3):1284–92. https://doi.org/10.1016/j.matdes.2009.09.011.

[3] Chu L, Li Q, Gu F, Du X, He Y, Deng Y. Design, modeling, and control of morphing aircraft: a review. Chin J Aeronaut 2022;35(5):220–46. https://doi.org/10.1016/j.cja.2021.09.013.

[4] Zhu J, Yang J, Zhang W, Gu X, Zhou H. Design and applications of morphing aircraft and their structures. Front Mech Eng 2023;18(3):34. https://doi.org/10.1007/s11465-023-0750-6.

[5] Ameduri S, Concilio A. Morphing wings review: aims, challenges, and current open issues of a technology. Proc Inst Mech Eng, Part C, J Mech Eng Sci 2023;237(18):4112–30. https://doi.org/10.1177/0954406220944423.

[6] Valasek J. Morphing aerospace vehicles and structures. In: Morphing aerospace vehicles and structures; 2012. p. 1–286. https://onlinelibrary.wiley.com/doi/book/10.1002/9781119964032.

[7] McGowan A-MR, Washburn AE, Horta LG, Bryant RG, Cox DE, Siochi EJ, et al. Recent results from NASA's morphing project. In: McGowan A-MR, editor. Smart structures and materials 2002: industrial and commercial applications of smart structures technologies. International society for optics and photonics, vol. 4698. SPIE; 2002. p. 97–111.

[8] Jenett B, Calisch S, Cellucci D, Cramer N, Gershenfeld N, Swei S, et al. Digital morphing wing: active wing shaping concept using composite lattice-based cellular structures. Soft Robot 2017;4:33–48. https://doi.org/10.1089/soro.2016.0032.

[9] De Gaspari A, Riccobene L, Ricci S. Design, manufacturing and wind tunnel validation of a morphing compliant wing. J Aircr 2018;55(6):2313–26. https://doi.org/10.2514/1.C034860.

[10] Fasel U, Keidel D, Baumann L, Cavolina G, Eichenhofer M, Ermanni P. Composite additive manufacturing of morphing aerospace structures. Manuf Lett 2020;23:85–8. https://doi.org/10.1016/j.mfglet.2019.12.004.

[11] Arena M, Amoroso F, Pecora R, Ameduri S. Electro-actuation system strategy for a morphing flap. Aerospace 2019;6(1). https://doi.org/10.3390/aerospace6010001.

[12] Dimino I, Concilio A, Schueller M, Gratias A. An adaptive control system for wing TE shape control. In: Farinholt KM, Griffin SF, editors. Industrial and commercial

applications of smart structures technologies 2013. International society for optics and photonics, vol. 8690. SPIE; 2013. p. 86900D.
[13] De Breuker R, Mkhoyan T, Nazeer N, Stuber V, Wang X, Mkhoyan I, et al. Overview of the smartx wing technology integrator. Actuators 2022;11(10). https://doi.org/10.3390/act11100302.
[14] Molinari G, Arrieta AF, Ermanni P. Aero-structural optimization of three-dimensional adaptive wings with embedded smart actuators. AIAA J 2014;52(9):1940–51. https://doi.org/10.2514/1.J052715.
[15] Molinari G, Quack M, Arrieta AF, Morari M, Ermanni P. Design, realization and structural testing of a compliant adaptable wing. Smart Mater Struct 2015;24(10):105027. https://doi.org/10.1088/0964-1726/24/10/105027.
[16] Haughn KPT, Gamble LL, Inman DJ. Deep reinforcement learning achieves multifunctional morphing airfoil control. J Compos Mater 2023;57(4):721–36. https://doi.org/10.1177/00219983221137644.
[17] Fichera S, Isnardi I, Mottershead JE. High-bandwidth morphing actuator for aeroelastic model control. Aerospace 2019;6(2). https://doi.org/10.3390/aerospace6020013.
[18] Grigorie TL, Botez RM, Popov AV, Mamou M, Mébarki Y. A hybrid fuzzy logic proportional-integral-derivative and conventional on-off controller for morphing wing actuation using shape memory alloy part 1: morphing system mechanisms and controller architecture design. Aeronaut J 2012;116(1179):433–49. https://doi.org/10.1017/S0001924000006977.
[19] Jodin G, Scheller J, Rouchon J-F, Braza M. On the multidisciplinary control and sensing of a smart hybrid morphing wing. In: 2017 IEEE international workshop of electronics, control, measurement, signals and their application to mechatronics (ECMSM); 2017. p. 1–6.
[20] Nazeer N, Wang X, Groves RM. Sensing, actuation, and control of the smartx prototype morphing wing in the wind tunnel. Actuators 2021;10(6). https://doi.org/10.3390/act10060107.
[21] Parancheerivilakkathil MS, Pilakkadan JS, Ajaj RM, Amoozgar M, Asadi D, Zweiri Y, et al. A review of control strategies used for morphing aircraft applications. Chin J Aeronaut 2024. https://doi.org/10.1016/j.cja.2023.12.035.
[22] Sun R, Yan D, Nangia RK, Cooper JE. Optimization design for aero-elastic morphing wings. In: Proceedings of 2017 9th international conference on modelling, identification and control, ICMIC 2017 2018-March; 2017. p. 25–30.
[23] Kammegne MJT, Grigorie LT, Botez RM, Koreanschi A. Design and wind tunnel experimental validation of a controlled new rotary actuation system for a morphing wing application. Proc Inst Mech Eng, G J Aerosp Eng 2015;230:132–45. https://doi.org/10.1177/0954410015588573.
[24] Khan S, Grigorie TL, Botez RM, Mamou M, Mébarki Y. Novel morphing wing actuator control-based particle swarm optimisation. Aeronaut J 2020;124:55–75. https://doi.org/10.1017/AER.2019.114.
[25] Botez RM, Kammegne MJ, Grigorie LT. Design, numerical simulation and experimental testing of a controlled electrical actuation system in a real aircraft morphing wing model. Aeronaut J 2015;119:1047–72. https://doi.org/10.1017/S0001924000011131.
[26] Popov AV, Grigorie TL, Botez RM, Mébarki Y, Mamou M. Modeling and testing of a morphing wing in open-loop architecture. J Aircr 2012;47:917–23. https://doi.org/10.2514/1.46480.
[27] Coutu D, Brailovski V, Terriault P, Mamou M, Laurendeau E. Real-time optimization of a research morphing laminar wing in a wind tunnel. In: Proceedings of the ASME conference on smart materials, adaptive structures and intelligent systems 2009, SMASIS2009, vol. 2; 2010. p. 203–9.
[28] Kammegne MJT, Botez RM, Grigorie LT, Mamou M, Mébarki Y. Proportional fuzzy feed-forward architecture control validation by wind tunnel tests of a morphing wing. Chin J Aeronaut 2017;30:561–76. https://doi.org/10.1016/J.CJA.2017.02.001.
[29] Ciminello M, Ameduri S, Concilio A, Dimino I, Bettini P. Fiber optic shape sensor system for a morphing wing trailing edge. Smart Struct Syst 2017;20:441–50. https://doi.org/10.12989/sss.2017.20.4.441.
[30] Shi X, Yang Y, Wang Z, Zhang S, Sun X, Feng W. Design and shape monitoring of a morphing wing trailing edge. Aerospace 2023;10(2). https://doi.org/10.3390/aerospace10020127.
[31] Roy R, Surace C, Gherlone M. An approach to morphing structure control based on real-time displacement reconstruction; July 2022.
[32] Gherlone M, Cerracchio P, Mattone M. Shape sensing methods: review and experimental comparison on a wing-shaped plate. Prog Aerosp Sci 2018;99:14–26. https://doi.org/10.1016/j.paerosci.2018.04.001.
[33] Paris D, Trevino L, Watson M. A framework for integration of ivhm technologies for intelligent integration for vehicle management. In: 2005 IEEE aerospace conference; 2005. p. 3843–52.
[34] Ko W, Richards WL, Fleischer VT. Applications of KO displacement theory to the deformed shape predictions of the doubly-tapered ikhana wing. https://api.semanticscholar.org/CorpusID:121877265, 2009.
[35] Esposito M, Mattone M, Gherlone M. Experimental shape sensing and load identification on a stiffened panel: a comparative study. Sensors 2022;22(3). https://doi.org/10.3390/s22031064.
[36] Mao Z, Todd M. Comparison of shape reconstruction strategies in a complex flexible structure. In: Tomizuka M, editor. Sensors and smart structures technologies for civil, mechanical, and aerospace systems 2008. International society for optics and photonics, vol. 6932. SPIE; 2008. p. 69320H.
[37] Ko W, Richards WL, Tran VT. Displacement theories for in-flight deformed shape predictions of aerospace structures. https://api.semanticscholar.org/CorpusID:107156918, 2013.
[38] Jutte CV, Ko W, Stephens CA, Bakalyar JA, Richards WL, Parker A. Deformed shape calculation of a full-scale wing using fiber optic strain data from a ground loads test. https://api.semanticscholar.org/CorpusID:137673671, 2013.
[39] Foss GC, Haugse ED. Using modal test results to develop strain to displacement transformations. In: Proceedings of the 13th international modal analysis conference. Society of photo-optical instrumentation engineers (SPIE) conference series, vol. 2460. 1995. p. 112. https://ui.adsabs.harvard.edu/abs/1995SPIE.2460..112F.
[40] Pisoni AC, Santolini C, Hauf DE, Dubowsky S. Displacements in a vibrating body by strain gage measurements. In: Proceedings of the 13th international modal analysis conference. Society of photo-optical instrumentation engineers (SPIE) conference series, vol. 2460. 1995. p. 119. https://ui.adsabs.harvard.edu/abs/1995SPIE.2460..119P.
[41] Bogert PB, Haugse E, Gehrki RE. Structural shape identification from experimental strains using a modal transformation technique. Collect Tech Papers - AIAA/ASME/ASCE/AHS/ASC Struct Struct Dyn Mater Conf 2003;3:2026–43. https://doi.org/10.2514/6.2003-1626.
[42] Rapp S, Kang L-H, Han J-H, Mueller UC, Baier H. Displacement field estimation for a two-dimensional structure using fiber Bragg grating sensors. Smart Mater Struct 2009;18(2):025006. https://doi.org/10.1088/0964-1726/18/2/025006.
[43] Tessler A, Spangler J. Inverse fem for full-field reconstruction of elastic deformations in shear deformable plates and shells. https://ntrs.nasa.gov/citations/20040086696, 2004.
[44] Tessler A, Spangler J. A least-squares variational method for full-field reconstruction of elastic deformations in shear-deformable plates and shells. Comput Methods Appl Mech Eng 2005;194(2):327–39. https://doi.org/10.1016/j.cma.2004.03.015.
[45] Kefal A, Oterkus E, Tessler A, Spangler JL. A quadrilateral inverse-shell element with drilling degrees of freedom for shape sensing and structural health monitoring. Eng Sci Technol Int J 2016;19(3):1299–313. https://doi.org/10.1016/j.jestch.2016.03.006.
[46] Roy R, Tessler A, Surace C, Gherlone M. Efficient shape sensing of plate structures using the inverse finite element method aided by strain pre-extrapolation. Thin-Walled Struct 2022;180:109798. https://doi.org/10.1016/j.tws.2022.109798.
[47] Roy R, Gherlone M, Surace C. A shape sensing methodology for beams with generic cross-sections: application to airfoil beams. Aerosp Sci Technol 2021;110:106484. https://doi.org/10.1016/j.ast.2020.106484.
[48] Nedelcu M. Optimisation of inverse finite element method for shape sensing of thin-walled cylinders by using generalised beam theory. Thin-Walled Struct 2023;188:110865. https://doi.org/10.1016/J.TWS.2023.110865.
[49] Craiu ID, Nedelcu M. Combining ifem and gbt for accurate shape sensing and damage detection in truncated conical shells with circular cross-section. Ocean Eng 2024;311:118811. https://doi.org/10.1016/J.OCEANENG.2024.118811.
[50] Esposito M, Roy R, Surace C, Gherlone M. Hybrid shell-beam inverse finite element method for the shape sensing of stiffened thin-walled structures: formulation and experimental validation on a composite wing-shaped panel. Sensors 2023;23(13). https://doi.org/10.3390/s23135962.
[51] Miller E, Manalo R, Tessler A. Full-field reconstruction of structural deformations and loads from measured strain data on a wing test article using the inverse finite element method. NASA/TM-2016-219407. https://ntrs.nasa.gov/citations/20160014695, 2016.
[52] Esposito M, Gherlone M. Composite wing box deformed-shape reconstruction based on measured strains: optimization and comparison of existing approaches. Aerosp Sci Technol 2020;99:105758. https://doi.org/10.1016/j.ast.2020.105758.
[53] Esposito M, Gherlone M. Material and strain sensing uncertainties quantification for the shape sensing of a composite wing box. Mech Syst Signal Process 2021;160:107875. https://doi.org/10.1016/j.ymssp.2021.107875.
[54] Kefal A, Oterkus E. Displacement and stress monitoring of a panamax containership using inverse finite element method. Ocean Eng 2016;119:16–29. https://doi.org/10.1016/j.oceaneng.2016.04.025.
[55] Kefal A, Oterkus E. Displacement and stress monitoring of a chemical tanker based on inverse finite element method. Ocean Eng 2016;112:33–46. https://doi.org/10.1016/j.oceaneng.2015.11.032.
[56] Savino P, Tondolo F. A new approach for displacement and stress monitoring of tunnel based on ifem methodology. Smart Mater Struct 2021;31(1):015013. https://doi.org/10.1088/1361-665X/ac3901.
[57] Savino P, Tondolo F. Two-node curved inverse finite element formulations based on exact strain-displacement solution. J Appl Comput Mech 2023;9(1):259–73. https://doi.org/10.22055/jacm.2022.41150.3708.
[58] Tessler A, Roy R, Esposito M, Surace C, Gherlone M. Shape sensing of plate and shell structures undergoing large displacements using the inverse finite element method. Shock Vib 2018;2018:1–8. https://doi.org/10.1155/2018/8076085.
[59] Zhao F, Bao H, Zhang F. Geometrically nonlinear deformation reconstruction of based on Euler–Bernoulli beam theory using a nonlinear ifem algorithm. Thin-Walled Struct 2023;189:110884. https://doi.org/10.1016/j.tws.2023.110884.
[60] Cerracchio P, Gherlone M, Di Sciuva M, Tessler A. A novel approach for displacement and stress monitoring of sandwich structures based on the inverse finite element method. Compos Struct 2015;127:69–76. https://doi.org/10.1016/j.compstruct.2015.02.081.

[61] Kefal A, Tessler A, Oterkus E. An enhanced inverse finite element method for displacement and stress monitoring of multilayered composite and sandwich structures. Compos Struct 2017;179:514–40. https://doi.org/10.1016/j.compstruct.2017.07.078.

[62] Kefal A, Diyaroglu C, Yildiz M, Oterkus E. Coupling of peridynamics and inverse finite element method for shape sensing and crack propagation monitoring of plate structures. Comput Methods Appl Mech Eng 2022;391:114520. https://doi.org/10.1016/j.cma.2021.114520.

[63] Ganjdoust F, Kefal A, Tessler A. Delamination detection and localization in vibrating composite plates and shells using the inverse finite element method. Sensors 2023;23(18). https://doi.org/10.3390/s23187926.

[64] Roy R, Gherlone M. Delamination and skin-spar debond detection in composite structures using the inverse finite element method. Materials 2023;16(5). https://doi.org/10.3390/ma16051969.

[65] Hexagon. Msc nastran 2022.4 quick reference guide; 2022.

[66] Berton B. Shape memory alloys application: trailing edge shape control. In: Multifunctional structures/integration of sensors and antennas; 2006:13. http://www.rto.nato.int/abstracts.asp.

[67] Wang DP, Bartley-Cho JD, Martin CA, Hallam BJ. Development of high-rate large-deflection hingeless trailing-edge control surface for the smart wing wind tunnel model. https://doi.org/10.1117/12.429682, 2001.

[68] Voss H. Regularization of least squares problems. https://www.mat.tuhh.de/lehre/material/RegLS.pdf, 2010. [Accessed 7 October 2023].

[69] Drela M. XFOIL: an analysis and design system for low Reynolds number airfoils; 1989.

[70] Roy R, Tessler A, Surace C, Gherlone M. Shape sensing of plate structures using the inverse finite element method: investigation of efficient strain–sensor patterns. Sensors 2020;20(24). https://doi.org/10.3390/s20247049.